THESIS FOR THE DEGREE OF LICENTIATE OF ENGINEERING

A Database of Microwave Single Scattering Properties of Ice Hydrometeors

Robin Ekelund

A Database of Microwave Single Scattering Properties of Ice Hydrometeors
Robin Ekelund

Cover:
Rendering of aggregate particles simulated in a stochastic fashion, meant to represent snow. The software used and details of the simulations are covered in paper A.

A Database of Microwave Single Scattering Properties of Ice Hydrometeors
Thesis for the degree of Licentiate of Engineering
Robin Ekelund
Department of Space, Earth and Environment
Chalmers University of Technology

Abstract

Microwave remote sensing by satellites is important for global observations of ice hydrometeors. Interpretation of the measurements requires sufficiently accurate knowledge of hydrometeors' interaction with photons, i.e. particle scattering and absorption. This presents a challenge for several reasons. Liquid hydrometeors can typically be modelled by spheroids, while the shapes of ice hydrometeors are known to be significantly more complex and variable. Also, the shapes can from a remote sensing perspective generally not be known exactly, as they vary from case to case. Finally, calculating the light scattering properties is challenging and computationally costly.

This thesis presents work related to recent efforts in improving the representation of light scattering by ice hydrometeors. A new single scattering database is presented, which includes 34 frequencies in between 1 and 874 GHz, and supports both passive and active microwave applications. A total of 34 different particle models were included, ranging from pristine crystals to aggregates. Complete random orientation is assumed throughout, slightly limiting its usefulness with respect to polarimetric measurements. Most aggregates were generated through simulation of aggregation, by letting particles collide randomly. The database can be considered the most extensive of this type to date, and future versions are intended to include oriented and melting particles. The general intention is to aid existing and future satellite retrievals, and satellite data assimilation into weather prediction models, all requiring accurate modelling of measured radiances. Special attention has been given to the upcoming Ice Cloud Imager (ICI), part of Europe's next generation of weather satellites.

Using the aggregation simulation tools developed for the database, a more dedicated case study was performed, which looked at the impact of different aggregate shape parameters on the resulting scattering properties. Both the amount and aspect ratio of the aggregate constituent crystals was found to have a high impact on both extinction (183, 325 and 664 GHz) and back-scattering (13, 36 and 94 GHz). Effective density and aerodynamic area had a high impact as well. Calculated radar triple frequency signatures were seen to clearly depend on the particle shape, consistent with previous studies. Overall, the results indicate that the particle shape should be considered in both passive and active applications above 13 GHz, and future database development will consider this. A potential application is also retrieval of ice particle shape through remote sensing.

Keywords: Ice hydrometeors, scattering properties, microwave, sub-millimetre, radar, remote sensing.

Acknowledgments

List of publications

This thesis is based on the following appended papers:

Paper A. P. Eriksson, R. Ekelund, J. Mendrok, M. Brath, O. Lemke, and S.A. Buehler (2018). "A general database of hydrometeor single scattering properties at microwave and sub-millimetre wavelengths". Earth System Science Data. Submitted.

Paper B. R. Ekelund and P. Eriksson (2018). "Impact of ice aggregate properties on microwave and sub-millimetre scattering properties". Journal of Quantitative Spectroscopy & Radiative Transfer. Manuscript in preparation.

Contents

Part I

Introductory chapters

Chapter 1

Introduction

1.1 Background

Clouds have a strong impact on the climate and have in recent years gained increased attention, in particular when it comes to high ice clouds. The fourth assessment of Intergovernmental Panel on Climate Change (IPCC) (IPCC, 2007) reported cloud response to climate change as one of the largest uncertainties. This assessment remains in the fifth and most recent assessment of IPCC where a new chapter on clouds and aerosols was introduced (IPCC, 2013), to further stress cloud importance.

The radiative budget of Earth is modified by clouds on one hand through absorption and reflection of sunlight, and on the other hand through reflection, absorption and emission of thermal infrared, either cooling or warming the planet. Cloud-radiation interaction is very strong and global cloud coverage on average is over two thirds of the earth (Wylie et al., 2005; Stubenrauch et al., 2013), thus a small shift in cloudiness can potentially have strong effect on the radiative budget. While liquid clouds interact strongly with both sunlight and infrared light, thin ice clouds interact mainly in the infrared, and have an either cooling or warming effect depending on the altitude. Low ice clouds emit radiation at a temperature roughly equal to the surface temperature, effectively cooling the atmosphere. As cloud altitude increases an increasingly warming effect is obtained, because the cloud gets colder and emit less, and a larger portion of the by atmosphere emitted radiation is trapped below the cloud. A shift towards higher and larger amounts of ice clouds could thus have strong impact on surface temperatures, for example. IPCC, (2013) suggests, based on General Circulation Models, (GCMs) and observations, that an increase in cloud height is likely in response to a warming climate. Hence, this type of mechanism may have an amplifying effect on a global temperature increase. Such processes are typically referred to as climate feedbacks, positive in this case. Multiple other cloud feedback mechanisms are possible, both positive and negative.

While the total cloud feedback is deemed likely positive by IPCC, (2013), there are significant uncertainties associated with clouds. One of the main issues is the representation of ice clouds, in particular that of ice cloud microphysics (McFarquhar et al., 2017). Cirrus (high altitude ice clouds) in particular remains a source of uncertainty in terms of feedback effects in GCMs (Baran, 2009). Ice particle

morphology, fall speed, aggregation, and other aspects, while mostly well investigated through laboratory experiments, are not well documented in nature. Understanding these aspects are vital in order understand and quantify ice cloud longevities, mass content, light-matter interaction and consequently the cloud impact on the radiative budget.

The importance ice hydrometeors (i.e. ice particles) for the hydrological cycle should be considered as well. Clouds are precursors to precipitation that in turn influence vegetation, storms, and weather in general. Of particular importance is understanding and being able to predict the annual cycles of the monsoon systems, which have an impact of a large fraction of the human population. Variations in yearly monsoon rainfall can have detrimental effects on agriculture, either due to a lack in rainfall or by causing floods (Webster et al., 1998). Ice particles are an important aspect to this, because liquid drops often originate from melted snow, initiated through the Wegener-Bergeron-Findeisen process (see Sec. 2.1.2).

On another note, assimilation of satellite passive microwave measurements of clouds and precipitation has recently become more important for weather forecasting. In fact, microwave sensors sensitive to humidity, clouds and precipitation have in only the recent 5 years risen to have the largest impact of all observation systems utilised by the European Centre for Medium-range Weather Forecasts (ECMWF) operational system (Geer et al., 2017). This is thanks to the information on the atmospheric dynamical state that the cloud and precipitation distributions provide. To summarize, the hydrological cycle, cloud radiative transfer, and atmospheric dynamics interact in a complex manner, making climate and weather prediction difficult. Understanding the role of ice hydrometeors in the atmosphere is a key component in improving this situation.

1.2   Atmospheric ice hydrometeors

Ice hydrometeors form through various processes at low enough temperatures, i.e. where the air is moist enough to the point of supersaturation with respect to ice (see Sec. 2.1.1). Special types of particles called ice nuclei (aerosols, minerals, sea spray, etc.) can enhance the ice particle accumulation by initiating freezing of supercooled liquid droplets upon contact or by providing a surface upon which ice can grow by deposition. Generally, ice supersaturation is achieved through lifting of an air parcel, consequently cooling it. Cirrus clouds form commonly through the lifting that occurs along warm fronts, but also in tropical deep convective cumulonimbus clouds. Through wind shear, an anvil-like structure is created, from which cirrus clouds break loose. Though the temperature at a given altitude is higher at low altitudes, i.e. in the tropics, cloud systems here also reach higher altitudes. The amount of cloud ice is thus by no means lower in the tropics. Fig. 1.1 exemplifies these kinds of processes. Other examples of processes through which ice hydrometeors form are the formation of snow through adiabatic cooling as air masses are pushed up against a mountainside (Baker and Lawson, 2006) or hail in the updrafts of deep convective systems.
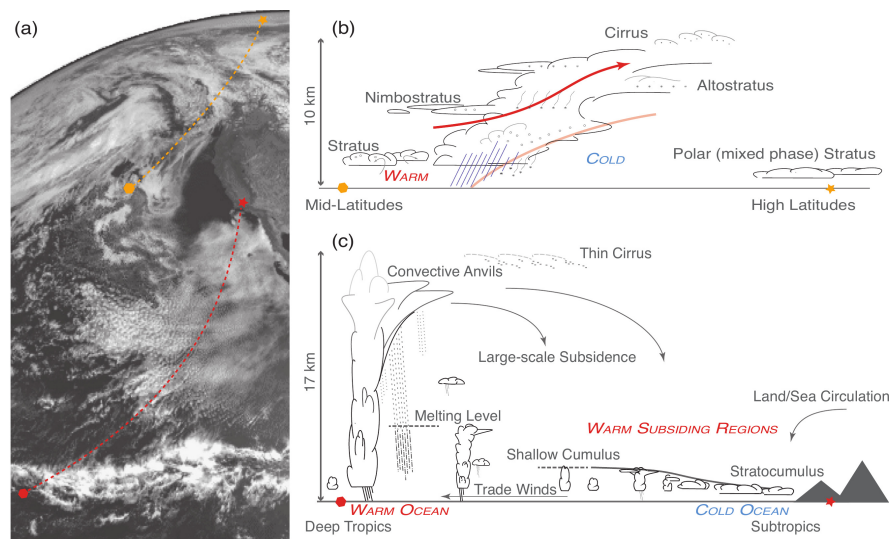
Figure 1.1: (a) Geostationary visible-wavelength image of a diverse set of cloud systems. (b) A schematic section along the yellow dashed line, trough an warm front of an extra-tropical cyclone. Several layers of cirrus are visible at the fore of the warm front. (c) Section along the red dashed line. A deep convective anvil system is seen to the left, with associated anvil cirrus. Figure is taken from IPCC, (2013).

1.3   Microwave remote sensing of atmospheric ice

While more and improved observational data by in-situ (direct) measurements is necessary for improving the knowledge on ice cloud microphysics, remote sensing (indirect measurements) is necessary in order to gain cloud observations on a temporally and spatially significant scale. Through satellite instruments, global coverage can be achieved over time-scales of several years. Several wavelength regions and techniques exist. Passive optical and infrared imagery can be used to directly measure radiative fluxes, but they give little information of clouds internal structure and water content, because the cloud penetration is limited. Active instrumentation, i.e. radar and lidar, has been used to measure water content specifically, including ice. The A-train constellation, a family of polar orbiting satellites, includes the CloudSat and Cloud-Aerosol Lidar and Infrared Pathfinder Satellite Observations (CALIPSO), carrying the Cloud Profiling Radar (CPR) and the Cloud–Aerosol Lidar with Orthogonal Polarization (CALIOP) aboard respectively (Stephens et al., 2002). The CPR which operates at large wavelengths (94 GHz, 3 mm) is sensitive to larger, precipitating ice particles and thick clouds. CALIOP operates in the infrared (1064 nm) senses smaller cloud ice particles and is therefore useful for measuring cirrus clouds. Conversely, radar is not sensitive to small particles and lidar has limited penetration capabilities beyond that of cirrus.

Down-looking passive microwave instrumentation currently utilize the frequency region in between 1 and 190 GHz. In contrast to lidar, microwave instruments have good penetration capabilities and are sensitive to snow, while less sensitive to the smallest ice particle sizes (Bühl et al., 2017). Because radars are limited to frequencies up to 94 GHz, high frequency passive microwave measurements in a sense fill the

gap between infrared (small ice cloud particles) and radar (large snow particles). The Global Precipitation Mission (GPM) mission (Hou et al., 2014) includes passive measurements up to 183 GHz, mainly suitable for precipitation, with a low sensitivity to smaller cloud ice particles.

Utilisation of microwave frequencies above 200 GHz, sensitive to the smallest ice particles (i.e. Cirrus cloud particles), is relatively in-mature. Observations of ice clouds using sub-millimetre frequencies has been demonstrated by the limb sounding missions Microwave Limb Sounder (MLS) aboard the Aura satellite (Wu et al., 2009) and the Sub-Millimetre Radiometer (SMR) on board the Odin satellite (Eriksson et al., 2014), which utilizes frequencies around 640 and 550 GHz respectively. The future MicroWave Imager (MWI) and Ice Cloud Imager (ICI) instruments on the Meteorological Operational Second Generation (MetOp-SG) satellites (Kangas et al., 2012) will perform observations at wavelengths between 0.45 mmand 1.6 cm, thereby extending down-looking passive microwave coverage to 670 GHz. Passive observations spanning this wavelength region result in sensitivity to ice hydrometeors over a broad size range, from cirrus crystals having a size of about 50 μm (Eriksson et al., 2008) to the largest snowflakes and graupel that exist (in the order of a few cm).

Aforementioned measurement systems are not complete without retrieval system, which in turn requires a forward model. Treating ice particles present three main issues. Firstly, ice particle scattering and absorption effects on measured radiation are non-trivial to quantify, due to the general complexity in terms of shape. Secondly, the ice particle shape is a property that varies significantly, within a given cloud and between different clouds. Thirdly, the particle orientation has an influence on the measured polarization signature.

In order to address above mentioned issues, there has been an effort from the remote sensing community to produce realistic parametrisations of single scattering properties (SSP) of ice particles. Because scattering properties of complex particles can not be calculated on the fly, tabulated data of simulated SSP is a necessity. A number of such databases has been produced during the last decade (Liu, 2008; Hong et al., 2009; Lu et al., 2016; Kuo et al., 2016; Ding et al., 2017). However, most of these databases are unsuitable for usage in the MetOp-SG instruments, for instance, due to limited frequency coverage. Furthermore, some of the databases make use of outdated refractive index models which deviate from more recent models. Finally, there is a lack of large complex aggregates, which mainly concerns the representation of ice precipitation.

1.4 Goal and thesis structure

The database issues discussed above are the main motivation for the work conducted in appended papers. The first paper A, presents a new single scattering database, intended to overcome previous database's aforementioned deficiencies, among others. Because the majority of the results produced in Paper A was produced in conjunction with an EUMETSAT study related to the MetOP-SG satellites mentioned above, there is an emphasis to the needs of those satellites in this thesis (ICI in particular). The second paper B, presents a case study where single scattering properties of

aggregates are investigated. In specific, the variation of scattering properties with respect to several aggregate parameters are analysed. The intention is to identify essential aspects relevant for radiative transfer and to guide future developments in databases.

The structure of the thesis is as following. Chapter 2 provides an overview of current knowledge of ice hydrometeors in terms of physics and observations that were relevant and considered in the development of the database presented in paper A. Chapter 3 introduces radiative transfer concepts required in order to contextualize the research presented in both papers A and B. Chapter 4, more technical in comparison, provides an overview of the current status of the field in terms of available scattering databases. Associated issues and gaps are identified for each respective database. Chapter 5 summarises the appended papers and gives a short outlook on future activities.

Chapter 2

Physics and observations of frozen hydrometeors

It is well known that the representation of ice particle scattering properties is important for radiative transfer modelling (e.g. Kulie et al., 2010; Geer and Baordo, 2014). Regarding microwave observations, calculations of single scattering properties at sub-millimetre frequencies especially, have shown high dependence on habit assumption (Hong et al., 2009; Liu, 2008) and strong shape-induced variance (Kuo et al., 2016; Nowell et al., 2013). The term habit refers to a group of particles that may occur in a range of sizes, but share a common morphology. For example, plate particles can be considered to be a single habit, though even more detailed divisions can be made (specific aspect ratios for instance). The variability of ice particles found in nature is in terms of size and morphology considerable. In the sixties, Magono and Lee, (1966) classified 80 different ice particle types based on observations mainly from Japan, a number still not high enough to cover the true variability in nature. Aggregates are not considered for instance. In a more recent study by Kikuchi et al., (2013), a total of 121 particles types were classified on a global basis, providing a more representative classification and illustrating the huge ice particle variability. An overview of ice particle physics relevant to characterize single scattering properties follows in the rest of this chapter.

2.1   Microphysics

Microphysics refers to areas of physics that study phenomena occurring at the microscopic scale (i.e. in the orders of μm). In the context of clouds, the growth and evolution of hydrometeors are studied. The morphology of ice particles is determined partly through the process in which they were nucleated, but mainly through the particle growth process. Ice particle growth can be divided into three main categories: growth by deposition, aggregation and riming. Following subsections cover the initial nucleation of ice particles and these three growth processes.

2.1.1   Ice particle nucleation

The creation of ice particles can occur through several ways. Supercooled liquid droplets (i.e. water droplets at temperatures below 0 °C) can freeze when it comes into contact with certain types of particles, called *freezing nuclei*, either already embedded in the droplet or by external contact. The freezing nuclei could be mineral dust, aerosols or any substance that promotes the freezing of supercooled water. The freezing nuclei initiates the freezing and creates an ice embryo, which grows until the whole droplet is frozen. This process is called *heterogeneous nucleation*. *Homogeneous nucleation*, where the ice embryo is formed spontaneously without the help of freezing nuclei, is possible as well. However, homogeneous nucleation requires relatively low temperatures, at least -35 °C, and thus generally only occur in high altitude clouds such as cirrus (Wallace and Hobbs, 2006). Finally, ice particles can also form through deposition onto ice nuclei directly, i.e. water vapour freezes directly onto the nuclei (no condensation involved). This requires that the air is supersaturated with respect to ice.

2.1.2   Growth by deposition

Particles generally grow through deposition, since ice supersaturation is generally much higher than the liquid water supersaturation at sub-zero temperatures (ice supersaturation pressure is lower than for water liquid). As an example, when the air is saturated with respect to liquid water at -20 K, the supersaturation with respect to ice is 21 %. In some conditions, commonly mixed-phase clouds, the air may be ice supersaturated and liquid water sub-saturated at the same time, resulting in evaporation of supercooled liquid droplets and the growth of ice particles through deposition, meaning that the ice particles grow at the expense of the liquid droplets (Wallace and Hobbs, 2006). This process is known as the Wegener-Bergeron-Findeisen process (Storelvmo and Tan, 2015) and is important for the initiation of precipitation.

The molecules of solid water form hexagonal lattice structures, which explains why pristine snowflakes typically have six arms or the hexagonal appearance of ice columns and plates. Other structures such as cubic lattices are possible at very low temperatures (< -80 °C), but in general, atmospheric ice take on the hexagonal lattice structure. Fig. 2.1 displays a set of example habits such as a hexagonal plate, column and bullet rosette. In contrast to popular belief, ice particles are generally found to be defective and irregular in shape (discussed in Sec. 2.4.2), while perfect dendritic snowflakes are rarities.

Studies in laboratory and by in-situ observations show that the manner in which ice particle grow in is influenced mainly by temperature and secondarily by ice supersaturation, effectively determining the ice crystal type (Bailey and Hallett, 2009). Fig. 2.2 demonstrates the variability of ice particle morphology with temperature and ice supersaturation. The figures originate from a combination of laboratory results and in-situ observations using a high resolution imager (Bailey and Hallett, 2009). As seen in the figure, depending on the temperature and saturation, observed ice crystals include columns, needles, plates, bullet rosettes (a particle consisting of bullet columns, connected at the tips), and the classical branched type of snowflake.

Figure 2.1: Examples of different habit classes: 1) plate, 2) bullet, 3) column (in this case, hollow column), 4) irregular, 5) rosette aggregate, 6) bullet rosette, 7) plate aggregates, and 8) column aggregate (Lindqvist et al., 2012).

Typically, for a given temperature, the complexity of the ice crystal increases with the supersaturation, going from compact plates or columns to dendrites and bullet rosettes. Furthermore, the habit diagram can be divided by temperature into regions where either plate-or column-like particles are formed. The dominant habit changes back and forth several times from plates to columns, at temperatures of roughly -4, -8 and -40 °C (plates below -4 °C and column-like above 40 °C). There is also division between single crystals and polycrystals at roughly -20 °C, with mixed rosettes of plate-like components above -40 °C and columnar rosettes below.

It should be noted that the particles displayed in Fig. 2.2 originate from controlled or relatively stable conditions. In reality, particles experience turbulence for instance, consequently growing in a range of different conditions. Resulting particles are thus often complex in shape, such as caped columns (columns with plates attached at the endpoints, see Fig. 2.3).

2.1.3 Growth by aggregation

Generally speaking, neither solid nor liquid particles grow large through deposition or condensation alone (Wallace and Hobbs, 2006). Through aggregation, ice particles can grow further by colliding into each other. While colliding raindrops coalesce into larger drops, ice particles and snowflakes are solid and may stick together. Fig. 2.3 shows a few examples of such particles in the lower row. Aggregation efficiency depends on temperature and crystal habit. Dendritic crystals aggregate efficiently thanks to their branched shape which allows them to interlock mechanically. Smoother ice crystals such as columns and plates can stick together due to electrostatic forces or surface melting, depending on temperature and relative humidity, but this mechanism is generally not as effective as dendrites interlocking. Aggregation sticking efficiency increases with temperature and is generally low below $-15°C$ (Hosler et al., 1957; Hobbs et al., 1974; Connolly et al., 2012). However, the efficiency is greatly enhanced at supersaturation with respect to ice regardless of temperature (Hosler et al., 1957).
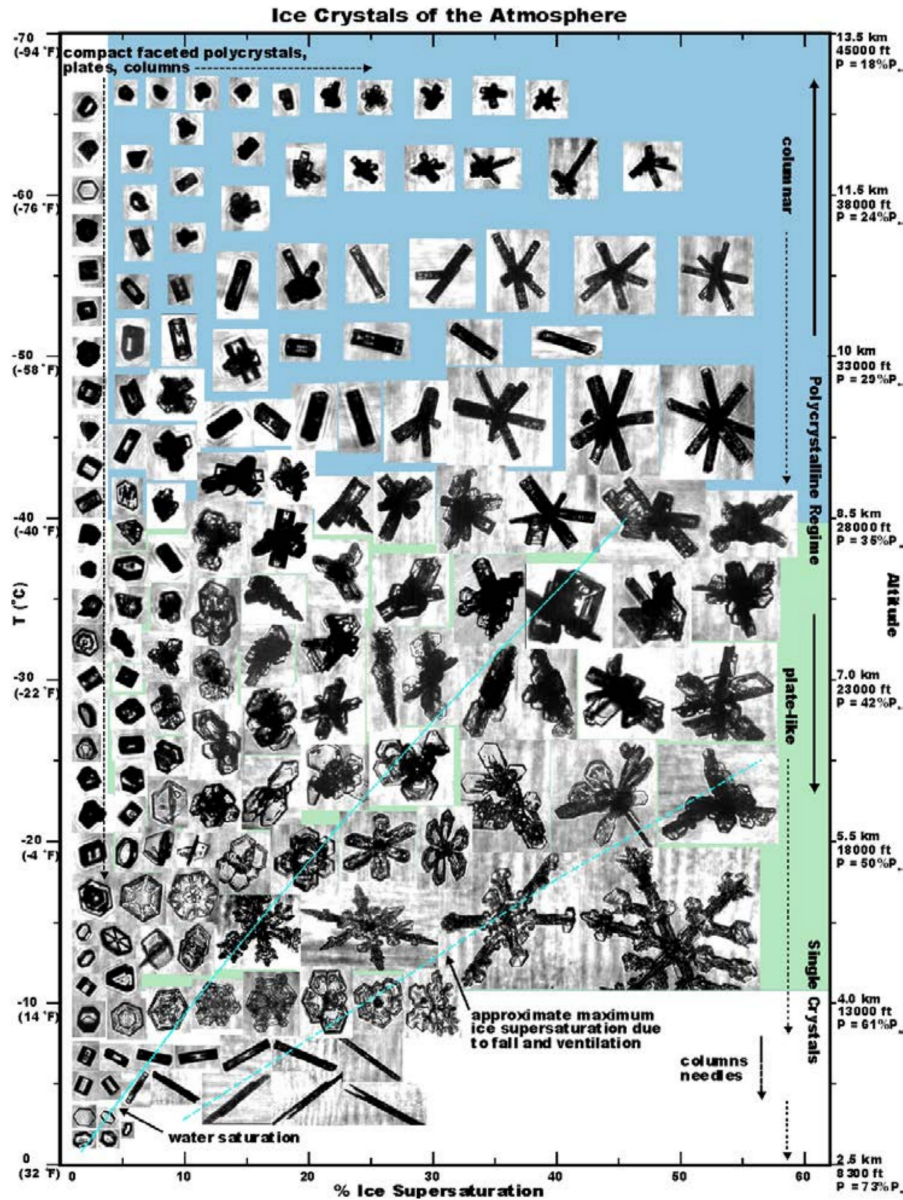
Figure 2.2: Habit diagram of ice crystals derived from laboratory results and CPI images obtained during AIRS II and other field studies. Right axis gives approximate height and pressure of ice crystal formation where P_0 is the standard atmosphere pressure. This figure is taken from Mitchell et al., (2011), where it was adapted from Fig. 5 of Bailey and Hallett, (2009).

2.1.4   Growth by riming

The third growth mechanism is riming. Ice particles and snowflakes can grow by colliding with supercooled water droplets that freeze immediately upon contact, forming small, spherical ice structures on the surface. Fig. 2.3 shows an aggregate that has undergone riming. As the degree of rime increases, the original particle becomes indiscernible, at which point it is referred to as *graupel*. Graupel usually takes on an either spherical or conical form. Riming can occur at temperatures
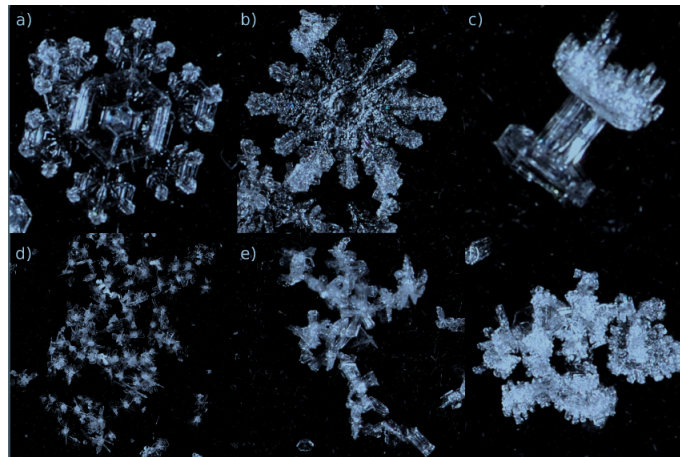
Figure 2.3: Examples of different types of single-crystals, aggregates and a rimed aggregate (not in the same scale). Top from left to right: a) branched sector plate, b) stellar crystals stacked on top of each other, c) rimed capped column. Bottom left to right: d) large aggregate of sector plates, e) aggregate of bullet rosettes, f) rimed aggregate snowflake. The images are from the GPM Cold Season Precipitation Experiment (Hudak et al., 2012).

down to about $-40°$C, where supercooled water can exist. As an indication of the importance of rime, contributions of $30-50\%$ to the total snowfall mass due to rime has been observed (Borys et al., 2003; Mitchell et al., 1990).

In vigorous convective clouds with high liquid water contents, riming can take the extreme form of hailstones. As the hail is bombarded with supercooled droplets at a high rate, latent heat released by freezing keeps the hailstone at a temperature close to zero. Collected droplets are thus prevented from freezing immediately, and form a wet surface. The liquid water either freezes slowly or is retained in internal cavities (Latham, 1969). Since the hail can be transported by up-and down-drafts several times, it may grow for a long time until the strength of the up-draft can no longer support the hailstone mass.

2.1.5 Melting ice particles

Scattering is also strongly affected by melting, due to the strong difference in dielectric properties of ice and liquid water, giving rise to the high radar reflectivities observed inside the melting layer, commonly referred to as the radar "*bright band*" (Fabry and Zawadzki, 1995; Wallace and Hobbs, 2006). Representing melting particles in a realistic fashion is a challenging task since morphology and melting processes are interdependent and not easily decoupled (Mitra et al., 1990; Oraltay et al., 2005; Tyynelä et al., 2014).

Several aspects influence the melting process of ice particles. When melting, faceted crystals such as plates tend to get covered in a liquid coating (Oraltay et al., 2005), while aggregates or dendrite snowflakes tend to form droplets influenced by surface tension. Due to differences in heat ventilation efficiency, melting is initially the most intense at the bottom (upwind) of the snowflake and at the less dense areas such as the tips of branches (Fujiyoshi, 1986; Mitra et al., 1990). The droplets

formed at the periphery may be shed from the snowflake. As the melting fraction increases, minimization of surface energy will concentrate droplets at certain areas, such as intersections between branches (Oraltay et al., 2005). Breakup will likely occur at high melting fractions if the mass distribution is strongly asymmetrical, i.e. when the particle is held together with only a few branches. As melting fraction increases further, ice structures will tend to collapse, until the particle is completely submerged into a droplet of water.

However there is still a lack of available observations or models quantifying the melting fractions important for characterising the radar bright band. This is of significant importance, as scattering simulations suggest that the melting fraction has a high impact on the scattering properties (Johnson et al., 2016).

2.2   Shape parametrisation and particle size distribution

Proper characterization of particles is required whether the issue is comparison studies, retrievals or modelling. This is not trivial and no unified standard exist when it comes parametrisation of ice hydrometeors. The following subsections give an overview of definitions and methods that are and have been used.

2.2.1   Size characterisation

Defining the size of a particle is often not straightforward. A cloud droplet is essentially spherical and well-defined by its diameter. In special cases such as with ice columns, the particle can be relatively well defined by its length and base diameter. However, ice particles generally do not conform to simple geometric shapes. Hence, there is a need for a more general way of parameterising particles, for the purpose of comparing scattering properties of different particles. Furthermore, models also require simplified and general parameterisations. A set of size parameters in use are described below.

The mass m is perhaps the most natural parameter for describing a particle and is also the most influential parameter regarding microwave scattering properties. An alternative parameter commonly used is the mass equivalent sphere diameter

$$D_{\mathrm{e}} = \left(\frac{6m}{\pi\rho}\right)^{1/3},\tag{2.1}$$

where ρ is the mass density. Commonly, ρ is the density of ice, meaning that D_{e} is the diameter of a mass equivalent ice sphere. Setting ρ as the density of liquid water has been used as well, in which case D_{e} can be viewed as the diameter of the particle melted to a liquid droplet (Petty and Huang, 2011). The mass does not give any indication of the shape of the particle, and is not the only aspect influencing particle scattering properties. Furthermore, the mass is not necessarily easily retrieved, especially for in-situ measurements based on 2D-images (see Sec. 2.4.1), where the full volume of the particles can not be directly measured.

The maximum dimension or diameter D_{max} is another parameter commonly used, since it is easily retrieved from 2D-images. It also gives an estimate of the extent of the particle. However, there is much ambiguity in the remote sensing and in-situ measurement community in how this parameter is defined. The parameter definition is mostly influenced by the nature of the given study or instrument, and it is often unclear what exact definition is actually used. In the case of in-situ 2D-imagery, the maximum dimension is usually defined as the maximum length found between two pixels. This definition is heavily dependent on the particle orientation during the image, resulting in a bias towards lower values since the true maximum dimension is unlikely to be be aligned with respect to the imager. Particle modellers can avoid this issue, either defining the maximum dimension as the maximum length between two surface points, or as the diameter of the minimum circumscribing sphere (in which case maximum diameter is a more proper term). Regardless of definition, it should hold that $D_{\mathrm{e}} \leq D_{\mathrm{max}}$, with equality only for spheres.

The relationship between mass and D_{max} depends on the exact shape and can not be specified by a single expression. However, the general behaviour of the mass for a given particle type or habit is commonly described by a mass-size relationship, which relates particle mass and maximum diameter by a power-law as

$$m = \alpha D_{\mathrm{max}}^{\beta}, \tag{2.2}$$

where α and β are adjustable relationship coefficients. The β-coefficient relates to how the particle is growing with size, while α relates to how dense or porous the particle is. A solid sphere has $\beta = 3$, while a plate that only grows along its edges has $\beta = 2$. For aggregates, β has been found to be normally close to 2. Westbrook et al., (2004) provided a theoretical argument for why this is the case. Columns and plates are usually observed having values $\beta \approx 2.5$ (Auer and Veal, 1970; Mitchell and Arnott, 1994; Um et al., 2015).

When considering a specific frequency, size parameter x is of importance as well. x describes the particle size compared to the wavelength of the radiation. The definition is:

$$x = \pi D / \lambda, \tag{2.3}$$

where λ is the wavelength. The diameter D can be either D_{e} and D_{max}. The general behaviour of single scattering depends strongly on this variable. Therefore, it is common to make the distinction between particles where $x \ll 1$, $x \approx 1$, or $x \gg 1$, referred to as the Rayleigh, Mie, and geometric optics regimes, respectively (see Sec. 3.2).

2.2.2   Aspect ratio

Aspect ratio (AR) provides a measure of the non-sphericity of a particle. It affects both the scattering properties and the particle orientation. Trying to express geometrical properties of a 3-dimensional (often irregular) structure by a two-number ratio, it is an inherently ambiguous and not clearly defined parameter. Accordingly, it is defined differently by different authors, and is also referred to as the axial

ratio. However, aspect/axial ratio can in general be taken as the ratio between the maximum dimension and the dimension in a perpendicular direction. The definition mainly deviates in exactly how the perpendicular direction is found. Many in-situ measurements just obtain a two dimensional view of the particle and the AR can only be roughly estimated (as the size in the third dimension is not known).

Cloud crystals below $D_{\max} = 1\,\mathrm{mm}$ demonstrate a large spread in aspect ratios, ranging from 1 to over 6, depending on crystal type (Um et al., 2015; Korolev and Isaac, 2003) Snowflake aggregates tend have a median aspect ratios between 1.5 and 2, while hail aspect ratio is close to 1 (Garrett et al., 2015). Riming shifts aspect ratio towards unity due to the particle acquiring an increasingly spherical shape.

The importance of aspect ratio when considering radiative transfer is mainly linked to how it affects particle orientation, which is discussed in Section 2.3.

2.2.3   Particle size distribution

Given a volume containing hydrometeors, particles do not occur in a single shape and size. Rather they exist in a range of different sizes and shapes. The particle size distribution (PSD) determines the total number of particles, mass and the scattering properties of a given volume element in the atmosphere. Hence, the PSD is of vital relevance in both numerical weather prediction and general circulation modelling as well as in radiative transfer modelling for remote sensing applications. While it might be possible to model particle evolution, i.e. size (and shape/habit) distributions from physical principles to some degree, in practice distribution data stems from observations, mostly from in-situ measurements (see Sec. 2.4). In the cloud and precipitation remote sensing community in general, a number of size distribution models are in use (e.g. Field et al., 2007; McFarquhar and Heymsfield, 1997).

Integration of the PSD N gives the total number density per volume element. Assuming that H different habits h with associated PSD:s N_h are present, the total number of particles per volume element is:

$$\sum_{h=1}^{H} \int_0^\infty N_\mathrm{h}(r)\,\mathrm{d}r, \tag{2.4}$$

where r denotes particle size. Weighting the PSD against a given quantity will produce so called bulk quantities. For example, assuming an extinction matrix $\mathbf{K}_\mathrm{h}$ (see Sec. 3.4) as function of r, the bulk extinction matrix is

$$\mathbf{K}_{avg} = \sum_{h=1}^{H} \int_0^\infty N_h(r)\,\mathbf{K}_\mathrm{h}(r)\,\mathrm{d}r. \tag{2.5}$$

Typically, size distributions are expressed using functional forms such as the gamma, modified-gamma, exponential or log-normal distribution (Petty and Huang, 2011).

2.3   Particle orientation

Single scattering properties depend not only on particle shape and composition, but also on the orientation. Particle orientation refers to how the particle is spatially
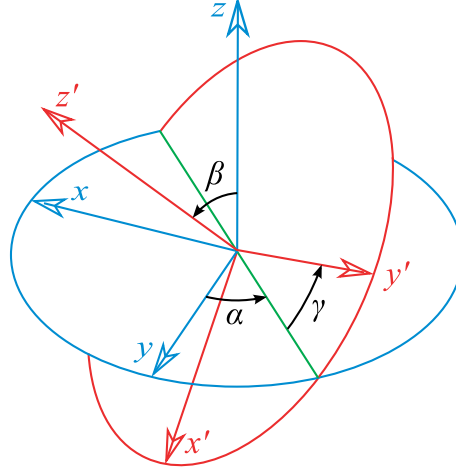
Figure 2.4: Euler angles. Drawing is taken from Yurkin and Hoekstra, (2014) and slightly modified.

aligned with respect to the local zenith and azimuth reference, and depends on the particle shape and surrounding atmospheric conditions. As an example, for a spherical liquid droplet, there is effectively no orientation due to its symmetries. Ice particles on the other hand, are generally non-spherical, and have in certain conditions preferred orientations. Several studies (Troitsky et al., 2003; Buehler et al., 2012; Xie et al., 2012; Defer et al., 2014; Gong and Wu, 2017) have shown that polarisation signals in passive microwave and sub-millimetre measurements emerge from oriented particles, which can be found in stratiform clouds and in convective clouds outside of the convective core, whereas the ice particles in convective cores are more likely randomly oriented.

In general, the orientation of a particle in a three dimensional space can be described by a set of three angles. The Euler angles define the orientation of the particle relative to a fixed coordinate system, often called the laboratory system. The particle system is the coordinate system that is attached to the particle. Commonly, the Euler angles according to the "zyz"-notation are used. The particle is first rotated by angle α over the laboratory Z-axis, then the particle is rotated by angle β over the particle Y-axis (Y'), and last the particle is rotated by angle γ over the particle Z-axis (Z'), see also Fig. 2.4. To clarify, the α-angle describes the azimuth rotation of the particle system relative to the laboratory system, the γ-angle the rotation of the particle around its own z-axis, and the β-angle the tilt of the particle relative to the laboratory system z-axis.

To add upon this, particles are in generally not found in a specific fixed orientation. Rather, the orientation of the particle can in general be considered random. Since we generally are interested in an ensemble of particles, an orientation distribution $p(\alpha, \beta, \gamma)$ must be be considered. For a given angular dependant SSP, such as the scattering matrix $\mathbf{Z}$ (see Sec. 3.2), the averaged quantity is

$$\mathbf{Z}_{\text{avg}}(\theta_i, \phi_i, \theta_s, \phi_s) = \int_0^{2\pi} \int_0^{\pi} \int_0^{2\pi} p(\alpha, \beta, \gamma) \, \mathbf{Z}(\theta_i, \phi_i, \theta_s, \phi_s, \alpha, \beta, \gamma) \, \sin\beta \, \mathrm{d}\alpha \, \mathrm{d}\beta \, \mathrm{d}\gamma,$$

$$(2.6)$$

where θ_i is the incidence polar angle, ϕ_i the incidence azimuth angle, θ_s the scattering polar angle and ϕ_s the scattering azimuth angle. The above expression is only valid for incoherent radiation, which is usually the case for atmospheric scattering and emission.

The question that remains is what $p(\alpha, \beta, \gamma)$ is. In reality this depends on multitude of circumstances such as winds and turbulence (Garrett et al., 2015), but also the shape and size of the particle itself. For a fluffy aggregate with an aspect ratio close to 1, one would expect that no specific orientation is more preferred than another. This is described by an uniform distribution, i.e.:

$$p(\alpha, \beta, \gamma) = \frac{1}{8\pi^2}. \tag{2.7}$$

The denominator is a normalisation coefficient, ensuring unity when integrating. This distribution is commonly referred to as random orientation, however this term is somewhat ambiguous, since there are other orientations that are random, just not necessarily uniform. Therefore, it will in the future be referred to as Totally Random Orientation (TRO). An illustration of TRO is available in Fig. 2.5.

In contrast, particles such as plates or dendrite snowflakes, would more likely align with its maximum area parallel to the horizontal plane as they sediment. Such an orientation is described by

$$p(\alpha, \beta, \gamma) = \frac{\delta\left(\beta\right)\delta\left(\gamma\right)}{2\pi}. \tag{2.8}$$

where δ is the Dirac delta function. The distribution thus describes particles constricted to lie in the horizontal plane, but are allowed to rotate around the zenith axis. The distribution is commonly referred to as horizontally random orientation (HRO). However, a more realistic assumption is that the particle does not lie perfectly in the horizontal plane, but experiences a certain degree of "fluttering". This is described by:

$$p(\alpha, \beta, \gamma) = \frac{p_\beta(\beta)}{4\pi^2}. \tag{2.9}$$

The α and γ angles are assumed uniformly distributed, while $p_\beta(\beta)$ describes a distribution of tilt-angles that the particles are realised in. Fig. 2.5 illustrates this orientation, here referred to as Azimuthally Random Orientation (ARO), where the particle is assumed to have a fixed tilt angle β. In reality, one would expect p_β to be described by a Gaussian distribution for instance, with a standard deviation depending on the given conditions.

To summarize, the particle orientation is essential when considering associated particle scattering properties. It is also important for atmospheric modelling when deriving particle fall-speed (and conversely precipitation rates). The particle orientation depends strongly on external factors such as turbulence, but perhaps more on the particle shape. Spherical particles will tend to totally random orientation, while high aspect-ratio particles such as dendrites will tend to a preferred orientation in the horizontal plane.
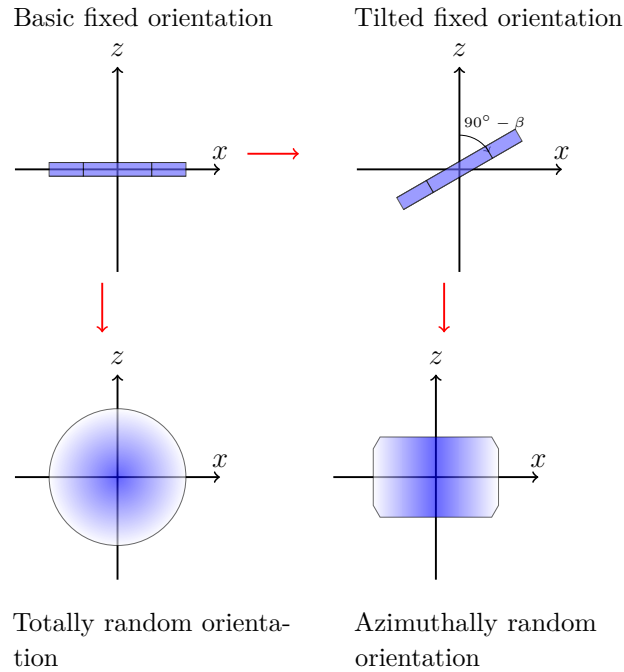
Figure 2.5: A schematic illustration of the difference between totally random (TRO) and azimuthally random orientation (ARO). (Top left) The particle in a fixed state, assumed to be a hexagonal plate (here seen from the side). (Bottom left) The particle in totally random orientation, effectively spherical with decreasing density outwards. (Top right) The particle in a fixed state, but with a tilt angle β applied. (Bottom Left) Azimuthally random orientation, i.e. rotation around the z-axis and the particle axis. The particle is effectively symmetric in the horizontal plane.

2.4 In-situ observations

Observations of ice hydrometeors are necessary in order to guide and validate modelling efforts. A multitude of measurement techniques are available, with associated strengths and weaknesses, suitable for varying scenarios and objectives. This section covers in-situ (direct) observations of ice particles.

2.4.1 Measurement techniques

In-situ measuring can be divided into groups of airborne and ground-based instrumentation. Airborne measurements have the obvious advantage of observing particles in atmosphere in various growth stages. As such, they are vital for improving the understanding of ice cloud microphysics. Airborne missions are relatively expensive in comparison to ground-based instrumentation however, and can only give observations for relatively short time frames.

A range of airborne sampling instrumentation is available. One family of instruments are the optical array probes (OAP), which function by illuminating particles with a collimated laser and imaging the particle shadows created. Instruments employing this method include the cloud particle imager (CPI) for high-resolution

imagery, two-dimensional stereo (2D-S) probes for stereoscopic images, and high-volume precipitation spectrometer (HVPS) for large particles (for details, the reader is referred to Baum et al., (2011)). These instruments can be operated both on-board aircraft and balloons. A particular problem with aircraft in-situ measurements is ice shattering that can occur around the inlet. This shattering of ice particles leads to an artificial increase in the concentrations of smaller ice crystals ($<100\,\mu$m), causing errors in the measured particle size distribution (PSD). This error has to be corrected (Field et al., 2006) or avoided by specially modified probe tips (Korolev et al., 2011). The problems with particle shattering on aircraft probes are avoided with balloon-borne measurements, as the ascent rate is slower (Kuhn and Heymsfield, 2016).

Ground-based instruments are able to locally measure microphysical properties such as fall speed, particle shape and size of snow and ice particles, but are limited to precipitating particles. Particle size velocity disdrometer (ParSiVel), hydrometeor velocity and shape detector (HVSD), two-dimensional video disdrometer (2-DVD), snowflake video imager (SVI), ground-based version of the aircraft CIP (GCIP), multi-angle snowflake camera (MASC), and ice crystal imaging (ICI) are examples of ground-based instruments that have been used to measure snow particles by making certain physical assumptions. A review of instruments specifications can be found in Kuhn and Gultepe, (2016).

2.4.2   Habit frequency

This section briefly discusses habit frequency observations reported in the literature. Since the amount and global coverage of in-situ observations are limited, it is difficult to obtain accurate statistics on the frequency of a given habit. However, some key observations are nonetheless prevalent. The observations considered here mainly include aircraft measurements, but cover all three main latitude bands, i.e. the tropics, mid-latitudes, and the Arctic. It does by no means represent a complete coverage of the current literature.

A key fact is the dominance of particles considered to be irregular (i.e. non-faceted single crystals), often about 90% of the particles observed for lower sizes (May et al., 2008; Um and McFarquhar, 2009; Zhang et al., 2013; O'Shea et al., 2016). As an example, Fig. 2.6 presents habit fractions of airborne observations (O'Shea et al., 2016) for mid-latitude cirrus clouds, where irregular (quasi-spherical) particles are seen to dominate in the lower region. Similar observations have been demonstrated for both tropical convective clouds and clouds in the Arctic, often with more than 90 % of observed particles being irregular (May et al., 2008; Um and McFarquhar, 2009; Korolev et al., 1999; McFarquhar et al., 2011). Exceptions exist however, in certain conditions pristine crystals can dominate (see Sec. 2.1.2). Orikasa et al., (2013) for example, found 45% single bullets in mid-latitude cirrus measured from balloons, with a marked lack of irregulars.

Fig. 2.6 otherwise shows that aggregates dominate at larger sizes, with rosettes claiming a large portion in decaying clouds as well. Baum et al., (2011) combined measurements from several field campaigns and saw similar importance of aggregates
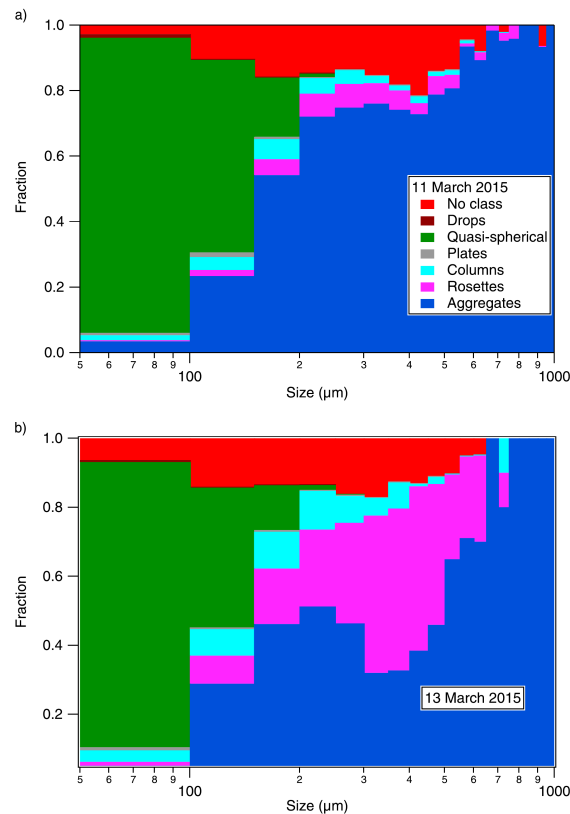
Figure 2.6: Habit fractions as a function of particle size for the cirrus sampling during two flights (a) developing cirrus cloud, and (b) decaying cirrus cloud (O'Shea et al., 2016).

for tropical deep convective ice clouds (anvil cirrus). The prevalence of aggregates at high altitudes is caused by the strong updrafts in deep convective cores, making it possible for large particles to exist at the top of the clouds.

2.4.3 Size ranges

Due to the different formation mechanisms, discussed in Section 2.1, the various observed frozen hydrometeor habits realistically occur over different size ranges. Table 2.1 displays typical habit size ranges based upon various sources from ground, balloon and aircraft measurements (Kajikawa, 1972; Heymsfield and Kajikawa, 1987; Lawson et al., 2001; Heymsfield and Miloshevich, 2003; Lawson et al., 2006; Baker and Lawson, 2006; Garrett et al., 2015; Um et al., 2015; O'Shea et al., 2016). The shown limits represent the largest values found in the literature, thus are not necessarily what one would observe in general. Nonetheless, some tendencies can clearly be observed. Single crystals tend to be limited to maximum dimensions below 2 mm, and spheroids are generally not observed at sizes larger than 200 μm. Crystals with arms (stellars, dendrites, etc.) occupy the middle region, roughly from 500 μm to 5.5 mm. Graupel and aggregates occupy a very broad size spectrum, from 100 μm to up to 5 cm. The broad size range is explained by the fact that there is a lack of a standard classification of aggregates (it includes everything from cirrus to snowflake

Table 2.1: Habit size ranges based on the observations discussed in the text. Values of D_{veq} are included when available.

Habit	$\min(D_{\mathrm{max}})$ [μm]	$\max(D_{\mathrm{max}})$ [μm]	$\max(D_{\mathrm{veq}})$ [μm]	$\max(D_{\mathrm{veq}})$ [μm]
Spheroid	< 10	200		
Thick plate	100	800	60	370
Irregular	10	1000		
Column	10	1,100		
Thin plate	100	1,500	70	530
Bullet rosette	100	1,600		
Stellar crystal	400	2,400	70	400
Fernlike crystal	800	4,300		
Dendrite crystal	550	5,600	120	680
Graupel	400	9,000	200	5,200
Aggregates	100	50,000		

aggregates). The aggregates reaching 5 cm were observed at ground (Newfoundland, Canada), and composed of dendrites and needles (Lawson et al., 2001).

Table 2.1 needs to be read with certain care. It is hard to set definite limits to the size for which a given habit can be observed in. Strictly speaking, when using analytical particle size distributions, sizes from zero to infinity should be covered (see Eq. (2.5)). However, the occurrence frequency of very large particles is so low as to be negligible. Furthermore, from a practical point of view it is sufficient to cover those parts of a size distribution that contribute to observable or modelled parameters – ice mass, mean particle size, total number of particles or simply the bulk scattering properties, which in turn depends on the actual application.

On the other hand, there are also issues with the measurements of the particle sizes as well as the classification of the habits. The sizes are mainly estimated from the maximum diameter in 2-dimensional cloud probe images where the extension in the third dimension remains unknown. This might bias maximum diameter measurements towards lower values. Finally, habit classifications often differ between sources, making it hard to compile consistent, generally valid and unambiguous habit size ranges.

Chapter 3

Atmospheric radiative transfer

Radiative transfer theory intends to describe the interaction of radiation propagation through some medium. The understanding of radiative transfer in the atmosphere is of key importance for both climate modelling and remote sensing. Through interaction with various gases, aerosols and hydrometeors in the atmosphere, radiation can be reflected, absorbed or emitted, with the relative importance of respective phenomena determined by the wavelength and type of particle. This chapter gives an overview of radiative transfer in the context of remote sensing, in particular when involving ice hydrometeors. Content is based primarily on Rees, (2012), Saleh and Teich, (2007), and Wallace and Hobbs, (2006)

3.1   Basic radiative transfer concepts

Light consists of electromagnetic waves which propagates at the speed of light c, as a consequence of Maxwell's equations. Except for the frequency ν, electromagnetic radiation is in essence characterized by three other properties: phase ϕ, intensity I and the polarisation. It is through these quantities that information can be retrieved through remote sensing. The quantities that are exploited depend on measurement technique and frequency region.

Radiation in the form of monochromatic (single wavelength radiation) electromagnetic waves are described by the complex valued electric field components

$$\mathbf{E}_v = \mathbf{e}_h E_{v0} \mathrm{e}^{-i(\omega t - kz - \phi_v)}, \tag{3.1}$$

$$\mathbf{E}_h = \mathbf{e}_v E_{h0} \mathrm{e}^{-i(\omega t - kz - \phi_h)}, \tag{3.2}$$

where it is assumed that the wave is propagating along the z-direction. Here, h and v denote horizontal and vertical polarisation, t the time, ω the angular frequency, k the wavenumber, and ϕ_h and ϕ_y the phases. ω is related to the cyclic frequency ν as $\omega = 2\pi\nu$ and k to the wavelength as $k = \frac{2\pi}{\lambda}$. Furthermore, it holds that the wavenumber is $k = \frac{\omega n}{c} = \frac{\omega}{c}\sqrt{\epsilon_r \mu_r}$, where $n = \sqrt{\epsilon_r \mu_r}$ is the refractive index, ϵ_r is the relative permittivity and μ_r the relative permeability of the given medium. Note that the speed of light in vacuum is $c = 1/\sqrt{\epsilon_0 \mu_0}$, where ϵ_0 and μ_0 are the permittivity

and permeability of vacuum, while the phase speed in a given medium is $v = 1/\sqrt{\epsilon\mu}$ where $\epsilon = \epsilon_r\epsilon_0$ and $\mu_r\mu_0$.

The permittivity and permeability are measures of a medium's response to an external electric and magnetic field, respectively, and they can both take on complex values. The consequence of this is that the refractive index and wavenumber can be complex-valued, i.e. $n = n_r + in_i$ and $k = k_r + ik_i = (n_r + in_i)\frac{\omega}{c}$. It follows then that Eq. (3.2) can be written as

$$\mathbf{E}_v = \mathbf{e}_v E_{v0}\mathrm{e}^{-k_i z}\mathrm{e}^{-i(\omega t - k_r z - \phi_v)}. \tag{3.3}$$

Apart from the fact that the wave now travels at a different speed, an attenuating exponential has been introduced, determined by the magnitude of n_i. Refractive indices of both frozen and liquid water vary strongly with frequency and exhibit a significant temperature dependence for microwave wavelengths. Also the ice lattice structure, i.e. hexagonal or cubic for example, has an impact. In order to characterize the refractive index at microwave frequencies and temperatures, numerous studies have performed measurements. For practical purposes (e.g. modelling), a number of sources of parametrised or tabulated data exist (e.g., Zhang et al., 2001; Jiang and Wu, 2004; Mätzler, 2006; Warren and Brandt, 2008).

The polarisation describes the geometric orientation of the electric field and how it varies with time, and is determined by the relative magnitudes of E_{v0} and E_{h0} and the phase difference $\Delta\phi = \phi_h - \phi_c$. A common way to describe the polarisation state and also the intensity, is through the Stokes vector (Mishchenko et al., 2002):

$$\mathbf{I} = \begin{bmatrix} S_0 \\ S_1 \\ S_2 \\ S_3 \end{bmatrix} = \frac{1}{2}\sqrt{\frac{\mu_0}{\epsilon_0}} \begin{bmatrix} \langle\mathbf{E}_{v0}\rangle^2 + \langle\mathbf{E}_{h0}\rangle^2 \\ \langle\mathbf{E}_{v0}\rangle^2 - \langle\mathbf{E}_{h0}\rangle^2 \\ \langle 2\mathbf{E}_{v0}\mathbf{E}_{h0}\cos(\Delta\phi)\rangle \\ \langle 2\mathbf{E}_{v0}\mathbf{E}_{h0}\sin(\Delta\phi)\rangle \end{bmatrix}, \tag{3.4}$$

where S_0 is equal to the flux density, i.e. the strength or intensity of the radiation (unit is $[\mathrm{W\,m^{-2}\,Hz^{-1}}]$). The remaining elements describe the polarisation state. In short, S_1 determines the degree of linear h-and v-polarisation, S_2 the linear $\pm 45°$ polarisation, and S_3 the left-and right-hand circular polarisation. The Stokes vector has the convenient property that assuming two incoherent waves (randomly changing phase difference), they can be added or decomposed linearly. Radiation in nature is generally incoherent. For example, in the atmosphere particles are positioned in a random fashion, i.e. scattered and emitted light will have random phase. Hence, in the context of passive microwave instruments which only detect intensity and polarisation, the Stokes vector is an useful parameter.

3.2 Scattering, absorption and extinction by particles

There are several ways of describing scattering properties of particles, depending partly by the generality required. Scattering, i.e. radiation whose propagation path

is directly altered by presence of the particle, can be described by the scattering cross-section σ_s. σ_s is scalar with the unit m^2, thus when given radiation of flux density S_0, the scattered energy is equal to $\sigma_s S_0$. The portion of light absorbed by the particle can in a similar fashion be described by the absorption cross-section σ_a. Furthermore, the total attenuation of the radiation is described by the extinction cross section σ_e, defined by

$$\sigma_e = \sigma_a + \sigma_s, \tag{3.5}$$

as a consequence of the conservation of energy principle.

However, σ_s gives no information on the angular distribution of the scattered radiation. In terms of the Stokes vector (Sec. 3.1), the angular distribution of the scattered radiation is described by the scattering matrix **Z** (size [4,4]):

$$\begin{bmatrix} S_0(r, \hat{\mathbf{n}}') \\ S_1(r, \hat{\mathbf{n}}') \\ S_2(r, \hat{\mathbf{n}}') \\ S_3(r, \hat{\mathbf{n}}') \end{bmatrix} = \frac{\mathbf{Z}(\hat{\mathbf{n}}', \hat{\mathbf{n}})}{r^2} \begin{bmatrix} S_0(r, \hat{\mathbf{n}}) \\ S_1(r, \hat{\mathbf{n}}) \\ S_2(r, \hat{\mathbf{n}}) \\ S_3(r, \hat{\mathbf{n}}) \end{bmatrix}. \tag{3.6}$$

where r is the distance to the particle, and $\hat{\mathbf{n}}'$ and $\hat{\mathbf{n}}$ the propagation vectors of the scattered field and incident field, respectively (Mishchenko et al., 2002). Note that it is assumed that $r \gg 0$, i.e. the equation describes scattering in the far field. **Z** is frequently denoted as the phase matrix, but scattering matrix (e.g. Bohren and Huffman, 1998) is a more descriptive name. σ_s is related to the scattering matrix by

$$\sigma_s = \int_{4\pi} \mathbf{Z}_{11} \, d\hat{\mathbf{n}}', \tag{3.7}$$

however other normalisations are in use. Assuming incoherence, Eq. (3.6) can be summed or integrated over multiple particles and orientations, for example using Eq. (2.5) and (2.6).

Scattering, absorption, and emission by particles are of fundamental importance for the radiative transfer of the atmosphere, whether by molecules, aerosols or hydrometeors. Atoms absorb and emit radiation at discrete energy levels predicted by quantum mechanics, i.e. electron orbits, while molecules also possess vibrational and rotational energies, depending on the molecules structure. These absorption lines have a finite width with respect to frequency, due to a number of line broadening processes. Natural broadening is due to the finite lifetime of the given excited state, and the inherent uncertainty in quantizing the energy. However, in the atmosphere, pressure broadening (particle collisions) and Doppler broadening are of much higher importance.

Macroscopic particles such as aerosols are composed of multiple molecules whose energy levels overlap with each other, creating a continuous absorption spectrum. Macroscopic particles can thus be treated according to electromagnetic theory, by considering the particle as a set of discrete electric dipoles. Parameters relevant here are the size parameter (see Eq. (2.3)), refractive index and the particle shape.

When the size parameter is small, i.e. $x \ll 1$ (particle is small compared to the wavelength), scattering can be derived by considering the particle as a single
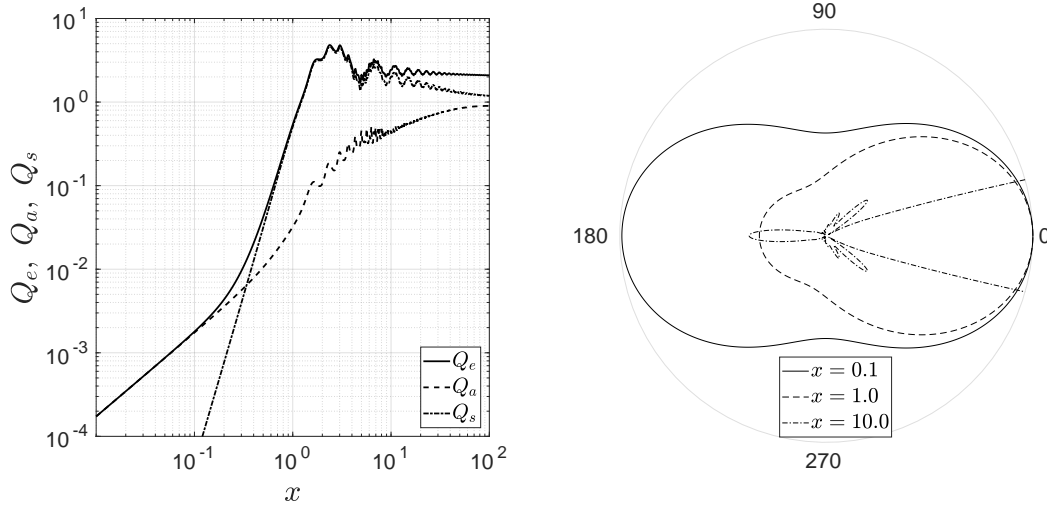
Figure 3.1: (Left) Extinction, scattering and absorption efficiency as a function
of size parameter, for an ice sphere. The refractive index is $n_{ice} = 1.78 + 0.011i$.
(Right) Angular scattering distributions ($\mathbf{Z}_{11}$) for ice spheres with three different
size parameters (normalized to fit in the plot). The $0°$ angle is defined as the
direction of the incident radiation. Note that only a small portion of the pattern
for $x = 10$ is displayed, since the forward lobe is very large in comparison to the
backward lobe.

dipole element, since the electric field of the radiation is roughly constant in space
at a given time. This regime is commonly referred to as the Rayleigh regime, and
the dependence on shape is relatively low. In the left panel of Fig. 3.1, extinction,
scattering and absorption efficiencies Q are plotted against x, assuming an ice sphere
at $439\,\mathrm{GHz}$. The extinction efficiency is given by

$$Q_e = \frac{\sigma_e}{\pi D_{\mathrm{veq}}^2}, \tag{3.8}$$

i.e. the cross-section normalized to the cross-sectional area of a volume equivalent
sphere. The scattering and absorption efficiency are defined in the same way. In the
Rayleigh regime ($x < 1$) absorption and scattering efficiencies are proportional to x
and x^4, respectively. The scattering is here relatively inefficient hence the extinction
is dominated by absorption.

The plot implies that ice particles in the Rayleigh regime should mostly absorb.
However, for other particles that may not be the case, depending on the dielectric
properties of the medium. For example, visible sunlight experience little absorption
by air molecules (due to lack of absorption lines at these frequencies), and is therefore
more affected by scattering, causing the blue color of the sky. Scattering of red
sunlight is because of the x^4-dependence inefficient in comparison, but can be observed
during sunsets when the path-length through the atmosphere is at its maximum. In
the right panel of Fig. 3.1 the scattering patterns of ice particles at three different
size parameters are visualized. The pattern for $x = 0.01$ is seen to consist of two
symmetrical forward and backward lobes of equal strength.

At size parameters $x \approx 1$, commonly referred to as the Mie regime, the single

dipole argument is no longer applicable, because the dipoles will no longer oscillate in phase in response to an external electric field. For homogeneous spherical particles, an analytic expression exists in the form of the Mie solutions (Mie, 1908):

$$Q_e = \frac{2}{x^2} \sum_{l=1}^{\infty} (2l+1)(|a_l^2| + |b_l^2|), \tag{3.9}$$

$$Q_s = \frac{2}{x^2} \sum_{l=1}^{\infty} (2l+1)\text{Re}(a_l + b_l), \tag{3.10}$$

where a_l and b_l are the Mie coefficients. Note that despite the name, the Mie equations are valid over all sizes, and are in fact approximately equal to Rayleigh scattering at small size parameters. In Fig. 3.1, oscillations are visible at $x > 1$, arising due to constructive and destructive interference of internally reflected fields in the sphere. Furthermore, extinction efficiency is now comparable to the cross-sectional area of the sphere. The fact that $Q_e > 1$ is possible is due to diffraction around the sphere edges. The angular scattering patterns in Fig. 3.1, left panel, are seen to increasingly favour forward scattering as x increases. At $x = 10$, the pattern is also seen to be more complex, with several side lobes visible. Size parameters $x > 50$ are usually referred to as the geometric optics regime, where the extinction converges to a constant value of 2.

For arbitrarily shaped particles, Rayleigh scattering is a good approximation at small size parameters. However, in the Mie region Eq. (3.9) and (3.10) are no longer valid, and numerical methods are required. An overview of such methods are provided in Sec. 3.5.

3.3   Thermal emission

All matter emits and conversely absorbs radiation at temperatures T above $0\,\text{K}$. A core concept in radiative transfer is the black body, which has the property that all incident radiation is absorbed. The emitted radiation is apart from the temperature dependent on the wavelength and is given by Planck's law, in terms of frequency ν:

$$B_{\nu,p} = \frac{2h\nu^3}{c^2 \left(e^{h\nu/kT} - 1\right)} \tag{3.11}$$

where $B_{\nu,p}$ (p denotes Planck) is the spectral radiance with unit $[\text{Wm}^{-2}\text{sr}^{-1}\text{Hz}^{-1}]$, h the Planck constant, k the Boltzmann constant. In Fig. 3.2 the Planck function is plotted for 300 and $6000\,\text{K}$, roughly the surface temperatures of Earth and the Sun respectively. As seen, the $300\,\text{K}$ curve peaks at roughly $30\,\text{THz}$ (thermal infrared) versus $6000\,\text{K}$ at $600\,\text{THz}$ (optical, blue).

While the Sun is relatively well approximated by a black body, it is still only a theoretical concept. Instead, the radiance B_ν of a particular medium can be related to the black body radiation through its emissivity ϵ as

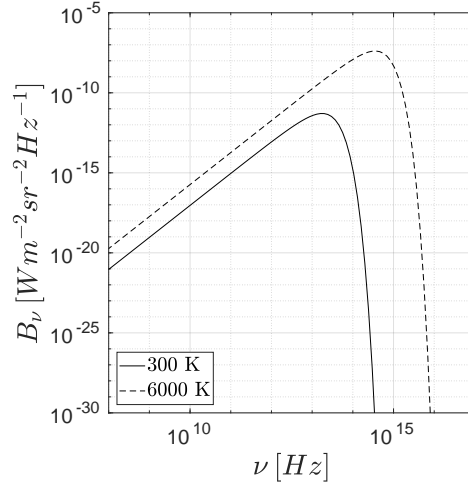$$B_\nu = \epsilon(\nu)B_{\nu,p}. \tag{3.12}$$

Figure 3.2: Planck's law in terms of frequency for two temperatures, 300 and 600 K.

According to Kirchhoff's law of thermal radiation, the emissivity is equal to the material's absorbance, i.e. the fraction of light absorbed by the material. This assumes local thermal equilibrium (LTE). Consequently, the emitted power from a particle with absorption cross section σ_a is $\sigma_a(\nu)B_{\nu,p}$.

3.4 The radiative transfer equation

Depending on the measurements to simulate, the optical properties of the atmosphere must be described to a varying degree of detail. The most detailed description is required for simulations of passive observations when the complete polarisation state is of interest, for example using the Stokes vector (Eq. (3.4)). The radiative transfer equation (RTE) to solve for such cases is:

$$\frac{\mathrm{d}\mathbf{I}(\nu,\mathbf{r},\hat{\mathbf{n}})}{\mathrm{d}s} = \underbrace{-\mathbf{K}(\nu,\mathbf{r},\hat{\mathbf{n}})\mathbf{I}(\nu,\mathbf{r},\hat{\mathbf{n}})}_{\text{Extinction}} + \underbrace{\mathbf{a}(\nu,\mathbf{r},\hat{\mathbf{n}})B_{\nu,p}(\nu,\mathbf{r})}_{\text{Emission}} \tag{3.13}$$
$$+ \underbrace{\int_{4\pi}\mathbf{Z}(\nu,\mathbf{r},\hat{\mathbf{n}},\hat{\mathbf{n}}')\mathbf{I}(\nu,\mathbf{r},\hat{\mathbf{n}}')\mathrm{d}\hat{\mathbf{n}}'}_{\text{Scattering}},$$

where s is the distance along $\hat{\mathbf{n}}$, $\mathbf{K}$ is the extinction matrix, $\mathbf{a}$ is the absorption vector and $\mathbf{Z}$ is the scattering matrix from Eq. (3.6). The extinction term is a sink term representing both the radiation scattered and absorbed away. The emission and scattering are source terms, representing the thermal radiation and radiation scattered into the propagation path. Also note that $\mathbf{K}$, $\mathbf{a}$ and $\mathbf{Z}$ here are bulk properties, i.e. they are integrated averages over a set of particles and orientations in the given volume element. See Mishchenko et al., (2002) for details regarding the assumptions for this equation and definitions of the involved quantities.

$\mathbf{K}$ is a 4 by 4 matrix and $\mathbf{a}$ is a vector of size 4, and are generalized quantities to σ_e and σ_a respectively (as $\mathbf{Z}$ is to σ_s). Analogously to Eq. (3.5), the energy conservation principle gives that $\mathbf{K}$, $\mathbf{Z}$ and $\mathbf{a}$ are related to each other by

$$\mathbf{K}_{i1} = \int_{4\pi} \mathbf{Z}_{i1} \, \mathrm{d}\hat{\mathbf{n}}' + \mathbf{a}_i. \tag{3.14}$$

where $\mathbf{K}_{i1}$ is the $(i, 1)$ element of the $\mathbf{K}$ matrix, etc.

In many situations it is possible to simplify Eq. (3.13) by considering fewer elements of the Stokes vector. This includes the case of "scalar radiative transfer" where the effective length of $\mathbf{I}$ is one, in which case $\mathbf{K}$, $\mathbf{a}$ are essentially replaced by σ_e and σ_a. The standard scalar representation of $\mathbf{Z}$ is the normalised phase function $P = 4\pi\mathbf{Z}_{11}/\sigma_{\mathrm{s}}$. Other simplified quantities are in use, such as the single scattering albedo ω_0, describing the fraction of the incident radiation that is scattered compared to the total attenuation, defined as

$$\omega_0 = \frac{\sigma_{\mathrm{s}}}{\sigma_{\mathrm{e}}} = \int_{4\pi} \mathbf{Z}_{11} \, \mathrm{d}\hat{\mathbf{n}}' \Big/ \mathbf{K}_{11}. \tag{3.15}$$

Purely scattering media, hence, have a single scattering albedo of 1.0, while $\omega_0 = 0.0$ indicates a purely absorbing medium. Asymmetry parameter g is a measure of the balance between forward ($\Theta < 90°$) and backward scattering ($\Theta > 90°$), and is defined as

$$g = \frac{1}{2} \int_{-1}^{1} \mu P(\mu) \, \mathrm{d}\mu, \tag{3.16}$$

where $\mu = cos(\Theta)$. Isotropic scattering results in $g = 0$. Values of g above zero correspond to a domination of forward scattering. Note in Fig. 3.1, right panel, g goes from 0 to 1 as x increases.

For radar measurements the main quantity required is the backscattering. The backscattering coefficient, for arbitrary polarisation, can be derived from $\mathbf{Z}$. The backscattering is essentially the scattering matrix value for the backward direction ($\hat{\mathbf{n}} = -\hat{\mathbf{n}}'$), that is backscattering is given by $\mathbf{Z}(-\hat{\mathbf{n}}, \hat{\mathbf{n}}')$. In the special case of macroscopically isotropic and mirror-symmetric particles, the scalar backscattering coefficient is given by

$$\sigma_{\mathrm{bac}} = \mathbf{Z}_{11}(\Theta = \pi). \tag{3.17}$$

The remaining part of radar simulations is to include the (two-way) extinction. This is done by the same $\mathbf{K}$ found in Eq. (3.13). Accordingly, radar simulations can be handled with the same set of optical properties as used in simulations of passive observations, and $\mathbf{K}$ and $\mathbf{Z}$ suffice to exhaustively describe all required parameters.

In summary, only absorption vector $\mathbf{a}$, extinction matrix $\mathbf{K}$ and scattering matrix $\mathbf{Z}$ are needed to describe the optical properties of particles in a general and complete manner[1]. These quantities can together be denoted as the single scattering properties (SSP).

---

[1]To be exact, $\mathbf{K}$ and $\mathbf{Z}$ suffice for a complete description as indicated by Eq. (3.14). However, deriving $\mathbf{a}$ from the other two is tedious and prone to numerical discretisation issues of the scattering matrix integral. Hence, it is common to provide all three parameters explicitly.

3.5   Single scattering calculation techniques

There are several methods for calculating scattering properties of particles at microwave frequencies. For the simplest case of a homogeneous or layered sphere, the exact solution can be provided by the Mie solution, as discussed Sec. 3.2. For complex morphologies, approximate methods are required. Methods common or used in studies and scattering databases are:

- T-matrix. Variants include:

  - Extended boundary condition method (EBCM)
  - The invariant imbedding T-matrix (II-TM)

- Discrete dipole approximation (DDA)

- Rayleigh-Gans theory

- Generalized multiple Mie (GMM)

- Improved geometrics optics method (IGOM)

The highly accurate T-matrix method (Waterman, 1965; Mishchenko et al., 1996) involves calculating the matrix which relates the expansion coefficients of the incident field to that of the scattered field. The advantage is that the T-matrix is not dependent on incident radiation direction, meaning that once it is calculated, scattering in any direction can be calculated analytically with the T-matrix as input. The T-matrix can be calculated in a number of ways. Waterman, (1965) used the Extended Boundary Condition Method (EBCM) that is based on solving the surface integral equations, which is suitable for symmetrical particles with smooth surfaces. The most widely used implementation of this method are likely the Mishchenko T-matrix routines (Mishchenko et al., 1996; Mishchenko and Travis, 1998). The Invariant Imbedding T-matrix (II-TM) (Schulz et al., 1998) solves the volume integral equation in an iterative manner. In general, T-matrix is an efficient option if the particle can be modelled in a simple fashion, especially if symmetries can be exploited (Kahnert, 2015). However, for complex morphologies computational time increases significantly, and the applicable size parameter range may also turn out to be severely limited.

In later years, the Discrete Dipole Approximation (DDA) method (Draine and Flatau, 1994) has become the most common method for calculating scattering properties of complex ice particles at microwave frequencies. The idea is to approximate the particle by a grid of polarisable points, and solve the resulting equation system. Its main advantage is that it treats arbitrary morphologies and is stable. It can be computationally very demanding though, and separate calculations must be performed for each required incidence angle (Kahnert, 2015).

Rayleigh-Gans theory assumes that the scattered field is the sum of the incidence field and the Rayleigh scattering by each volume element (Hulst, 1957). This method is computationally fast, but it does not consider coupling between volume elements

and is thus unsuitable for dense particles at moderate and large size parameters. The Generalized Multiple Mie (GMM) method instead approximates the particle by a set of spheres and uses extended Mie-theory to calculate the scattering properties (Xu, 1995). This method takes coupling between spheres into account, but imposes a drastic change in morphology which may need to be compensated for by modifying the density and dielectric properties of the material (Lu et al., 2016). For cases with large size parameters, one can use the Improved Geometrics Optics Method (IGOM) which is based on ray-tracing (Yang and Liou, 1996). Further methods exist (Kahnert, 2015), but focus has been put on methods relevant to studies examined in the next chapter.

Chapter 4

Existing scattering databases

Several attempts have been made at producing publicly available databases of single scattering properties for ice hydrometeors at microwave frequencies. They differ in characteristics such as frequency coverage, habits and sizes covered, simply due to difference in target applications. The five most extensive publicly available databases are: Liu, (2008), Hong et al., (2009), Kuo et al., (2016), Lu et al., (2016) and Ding et al., (2017). An overview of each database is found in Tables 4.1 – 4.5. Note that D_{max} is the maximum dimension and D_{veq} is the volume equivalent diameter. To give a clue on how shape varies with size, tables include mass-size relationship coefficients α and β when available (see Sec. 2.2.1).

It becomes clear when browsing the databases, that while impressive in some aspects, none covers the needs of the Ice Cloud Imager (ICI) instrument, for instance (a requirement for the database produced in paper A). The biggest limitation of these databases lies in the frequency coverage. The frequency range of MWI, MWS, and ICI goes from 18.7 to 668.2 GHz, which only Ding et al., (2017) cover fully. Also, except for the Lu et al., (2016) database, only random particle orientation is considered. This is not a realistic assumption for particles with high aspect ratios, and it also means that polarimetry information is lost (which some of the MWI, MWS and ICI channels are designed to provide). Considering the prevalence of irregulars as discussed in Sec. 2.4.2, one could also discuss how well they are considered or covered by these databases, which are mostly focused towards pristine crystals. The same argument applies somewhat for bullet rosettes, which are only covered extensively by the Liu, (2008) database. Also, both of the databases by Hong and Ding make use outdated models for the refractive index (for details, see Sec. 4.2 and 4.5, respectively).

4.1 Liu database

The Liu, (2008) database characteristics are summarized in Table 4.1. It is limited in habits to idealized hexagonal crystals and two idealized snowflakes, albeit at relatively large size ranges (compare to size ranges presented in Section 2.4.2). Note that the column and plate crystals all have values $\beta = 3$, which indicates that aspect
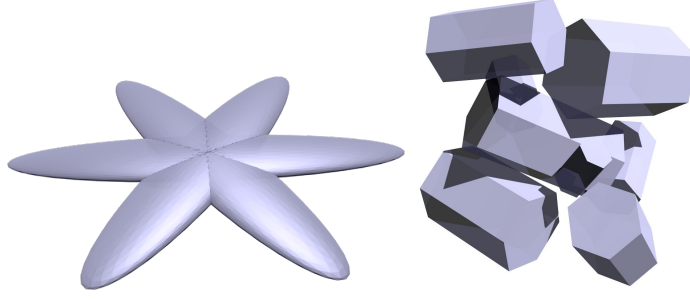
Figure 4.1: (Left) Sector snowflake in Liu, (2008) composed of three ellipsoids with a shared center. (Right) Aggregate in Hong et al., (2009), composed of eight hexagonal columns stuck together. Figures are rendered using Blender

.

ratios are fixed with respect to $D_{\max}$. This is not a realistic assumption, observations indicate values of β close to 2.5 as mentioned in Section 2.3.

More realistic mass-size relationships are observed for the bullet rosettes and snowflakes, with $\beta \approx 2.3$ and $\beta \approx 1.5$ respectively. See Fig. 4.1 for a rendering of the sector snowflake. Its mass-size relationship is based on measurements reported in Heymsfield et al., (2002) and Heymsfield and Miloshevich, (2003). Geer and Baordo, (2014) and Eriksson et al., (2015) argued for the sector snowflake as a good candidate for representing average scattering properties, albeit judged based on a limited set of reference data. Finally, considering the prevalence of bullet rosettes in nature, it is suitable that several bullet rosette habits have been considered. However, only rosettes with perpendicular arms are covered, even though this is generally not the case in nature.

4.2   Hong database

Table 4.2 presents the database by Hong et al., (2009), which like the Liu, (2008) database is limited to single crystal habits (we consider the bullet rosette a single crystal), with the exception of one aggregate. The aggregate model is an idealized representation, where 8 hexagonal columns of different sizes have been stuck together in a random fashion (see Fig. 4.1 for a visualization). As indicated by the value $\beta = 3$, all three dimensions behave equally over all sizes, an unrealistic assumption as mentioned above. At sizes of $D_{max} \approx 2\,\mathrm{mm}$ one might regard this particles as hail or a pellet, rather than something snowflake-like (as discussed in Section 2.1.4). The other habits demonstrate more realistic β values. While having an impressive frequency range in the upper end, it lacks frequencies below 90 GHz. It is furthermore limited by its usage of an outdated refractive index model Warren, (1984), which Eriksson et al., (2015) showed to produce systematic biases in absorption. Also, only one temperature is covered, which only furthers the point that absorption is not well characterised by this database. Finally, the maximum sizes in the database are relatively low, consistently below $2000\,\mu\mathrm{m}$ in $D_{\max}$. This is reasonable in the case of the single crystal habits (see size ranges in Section 2.4.3), but not realistic for aggregates and inhibits its use for modelling of precipitating ice.

Table 4.1: Overview of the Liu, (2008) database. Note that many of the listed frequencies have been added post publication (10 frequencies originally).

Database:	Liu, (2008)
Products provided:	Scattering cross section, absorption cross section, backscattering cross section, asymmetry parameter, phase function
Orientation:	Random
Refractive index:	Mätzler, (2006)
Frequencies [GHz]:	3, 5, 9, 10, 13.4, 15, 19, 24.1, 35.6, 50, 60, 70, 80, 85.5, 90, 94, 118 150, 166, 183, 220, 340
Temperatures [°C]:	$-40, -30, -20, -10, 0$
Computational method:	DDA

Habits	Number of sizes	Range of D_{max} [μm]	Range of D_{veq} [μm]	α	β
Long columns	7	$121-4,835$	$50-2,000$	33.999	3.000
Short columns	7	$83-3,304$	$50-2,000$	106.555	3.000
Block columns	7	$66-2,632$	$50-2,000$	210.276	3.000
Thick plates	7	$81-3,246$	$50-2,000$	112.303	3.000
Thin plates	7	$127-5,059$	$50-2,000$	29.673	3.000
3-bullet rosettes	20	$50-10,000$	$37-2,172$	0.182	2.275
4-bullet rosettes	20	$50-10,000$	$39-1,968$	0.110	2.237
5-bullet rosettes	20	$50-10,000$	$41-2,116$	0.140	2.242
6-bullet rosettes	20	$50-10,000$	$42-2,246$	0.175	2.251
Sector snowflake	20	$50-10,000$	$50-1,343$	0.001	1.471
Dendrite snowflake	20	$75-12,454$	$67-1,677$	0.003	1.734

Table 4.2: Overview of the Hong et al., (2009) database.

Database:	Hong et al., (2009)
Products provided:	Extinction efficiency, single scattering albedo, asymmetry parameter, scattering phase matrix
Orientation:	Random
Refractive index:	Warren, (1984)
Frequencies [GHz]:	90.0, 118.0, 157.0, 166.0, 183.3, 190.0, 203.0, 220.0, 243.0, 325.0, 340.0, 380.0,425.0, 448.0, 463.0, 487.0, 500.0, 640.0, 664.0, 683.0, 874.0
Temperatures [°C]:	-30
Computational method:	DDA

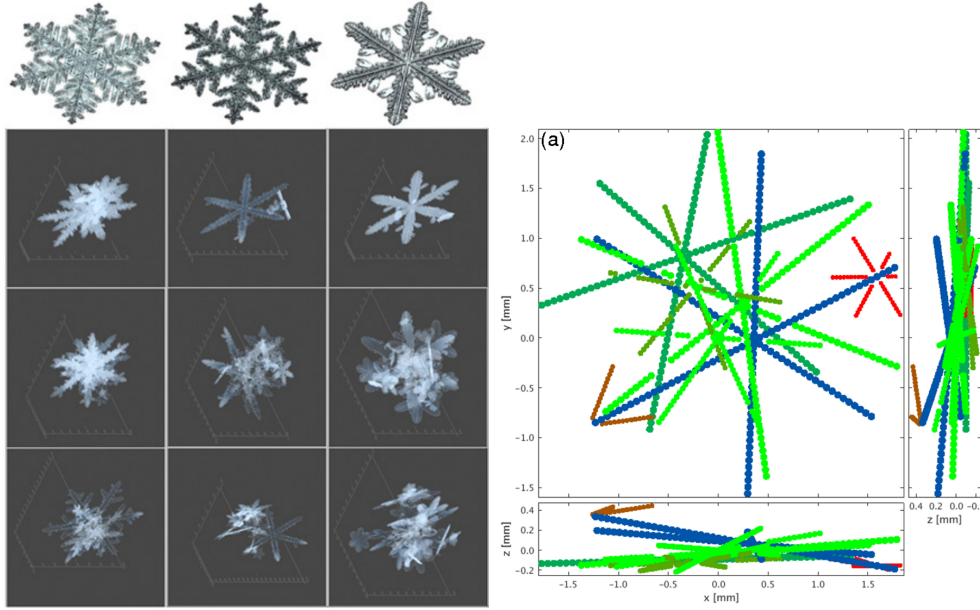| Habits	Number of sizes	Range of D_{max} [μm]	Range of D_{veq} [μm]	α	β
Hexagonal column	38	$2-2,000$	$1.7-621.8$	0.029	2.000
Hexagonal plate	38	$2-2,000$	$70.0-688.4$	0.745	2.474
Hollow hexagonal column	38	$2-2,000$	$97.0-616.0$	0.028	2.000
6-bullet rosette	38	$2-2,000$	$60.4-566.8$	0.305	2.420
8-column aggregate	38	$2-2,000$	$2-1,795$	347.162	3.000
Droxtal	38	$2-2,000$	$1.8-1,795.3$	347.2	3.000

Figure 4.2: (Left) Examples of crystals and aggregates used in the Kuo et al., (2016) database (figure taken from Kuo et al., 2016). (Right) Example of a GMM realization of a stellar aggregate used in the Lu et al., (2016) database with top and side views (figure taken from Lu et al., 2016).

4.3   Kuo database

The database developed by Kuo et al., (2016) (Table 4.3) is, in comparison to the above ones, an attempt to model both snowflakes and aggregates using semi-realistic simulations. The pristine crystals are modelled by a computational algorithm developed by Gravner and Griffeath, (2009) that simulates snowflake growth. By varying supersaturation, initial crystal seed, etc., crystals similar to observations can be produced. The aggregates are constructed in a stochastic fashion, using the pristine crystals as building blocks. Component particles are assumed to lie in the horizontal plane when aggregated, with some tilt variance. This results in aggregates with relatively high aspect ratio, though only random orientation is considered for the scattering properties themselves. Examples of pristine crystals and corresponding aggregates are shown in Fig. 4.2, left panel. Unfortunately, neither the phase nor the scattering matrix is provided, only cross sections and asymmetry parameter are available. This limits its applicability to simplistic radiative transfer modelling approaches. It is also unclear what temperatures or refractive indices are used. Nonetheless, the quantity of complex crystals and aggregates (a total of 6646 shapes) is impressive, and they are shown to agree well with in-situ mass-size relationships (Heysmfield et al., 2010). The size ranges are also large, up to 1.4 cm.

4.4   Lu database

In Table 4.4 the database by Lu et al., (2016) is presented, which also treats aggregates. It does not cover as many aggregates as Kuo, and the crystals are represented by

Table 4.3: Overview of the Kuo et al., (2016) database. Note that the database provides data for both single crystals and corresponding aggregates. The size ranges listed here refer that of the aggregates. The single crystals do not reach the same sizes, in general the maximum D_{veq} is between 1000-2000 μm.

Database:	Kuo et al., (2016)
Products provided:	Scattering cross section, absorption cross section, backscattering cross section, asymmetry parameter.
Orientation:	Random
Refractive index:	(unclear)
Frequencies [GHz]:	3.00, 5.00, 10.66, 13.61, 18.71, 23.82, 35.53, 89.06, 94.07, 94.07, 150.10, 165.62, 176.42, 180.43, 186.43, 190.43
Temperatures [°C]:	0 (ambiguous)
Computational method:	DDA

Habits (aggregate versions)	Number of sizes	Range of D_{max} [μm]	Range of D_{veq} [μm]
Fern dendrite	465	260 – 14,260	164 – 3,100
Classic dendrite	399	260 – 14,260	164 – 3,100
Dendrite with facets	266	260 – 14,260	164 – 3,100
Simple star-shaped dendrite	465	260 – 14,260	164 – 3,100
Needle	465	260 – 14,260	164 – 3,100
Dendrite with broadening arms v.1	997	260 – 14,260	164 – 3,100
Dendrite with broadening arms v.2	997	260 – 14,260	164 – 3,100
Dendrite with broadening arms v.3	997	260 – 14,260	164 – 3,100
Sandwich plate	997	260 – 14,260	164 – 3,100

idealized cylinders or plates. The aggregates are composed of either needles or stellar crystals. Also, the aggregation process is constrained to an aspect ratio of 1.7 and mass-size relationships reported by Mitchell, (1996). This results in relatively flat aggregates in the upper size range, as seen in Fig. 4.2.

The database differs in several ways compared to previous cases. Firstly, it is calculated for fixed instead of random orientations, implemented by fixing the particle in the horizontal plane and shifting the incidence angles by increments of 10° in zenith and azimuth. This means that polarimetric information is conserved. However, problems may arise since the incidence angle grid is coarse at large size parameters, i.e. interpolation between grid points will produce large errors, and it may be hard to compute average properties accurately. Secondly, the DDA method has been replaced by the GMM method for calculating the scattering properties of aggregates. For some of the pristine crystals, both GMM and DDA were used. Discrepancies are reported between the two methods, but are argued to be smaller than the variance induced by shape variance. The database also makes use of the long outdated refractive index model by Ray, (1972) at only one temperature of 0 K. A short review available in paper A, shows that this model deviates significantly from more recent models. It is unclear what the motivation for this choice was, as it severely mismodels the imaginary part as stated in the publication. Finally, the database is currently limited to only 4 radar frequencies.

Table 4.4: Overview of the Lu et al., (2016) database.

Database:	Lu et al., (2016)
Products provided:	Amplitude scattering matrix, scattering cross section, absorption cross section, backscattering cross section, asymmetry parameter, etc.
Orientation:	Fixed (multiple incidence angles with increments of 10° in zenith and azimuth)
Refractive index:	Ray, (1972)
Frequencies [GHz]:	9.4, 13.4, 35.6, 94
Temperatures [°C]:	0
Computational method:	DDA and GMM

Habits	Number of sizes	Range of $D_{\max}$ [μm]	Range of D_{veq} [μm]
Aggregates	660	$580 - 62{,}580$	
Branches planar crystals	405	$500 - 5{,}630$	
Plates	44	$100 - 2{,}520$	
Columns	30	$180 - 4{,}310$	
Conical graupel	640		$200 - 2{,}500$

4.5   Ding database

The Ding et al., (2017) database is displayed in Table 4.5. It serves as an extension of the database presented in Yang et al., (2013), which considered ultraviolet to far-infrared frequencies. Several of the habits used here are of the same parametrisation as the Hong et al., (2009) database (column, hollow column, plate, bullet rosette and 8-column aggregate). Similarly to the aggregate by Hong et al., (2009), all aggregate habits here have $\beta = 3$, hence the included habit models can not be considered as sophisticated as in the Lu et al., (2016) and Kuo et al., (2016) databases. Nonetheless, it covers a wide and highly resolved range of frequencies up to 874 GHz, large sizes up to 10 mm, four temperatures with a modern refractive index model (Iwabuchi and Yang, 2011) and provides the full phase matrix, but for totally randomly oriented particles only. The scattering properties were calculated primarily using II-TM (Schulz et al., 1998), though IGOM (Yang and Liou, 1996) was used for the largest size parameters.

Table 4.5: Overview of the Ding et al., (2017) database.

Database:	Ding et al., (2017)
Products provided:	Phase matrix, extinction efficiency
	asymmetry factor, single scattering albedo
Orientation:	Random
Refractive index:	Iwabuchi and Yang, (2011)
Frequencies:	41 frequencies between $1-874\,\mathrm{GHz}$
Temperatures [K]:	160, 200, 230, 270
Computational method:	II-TM and IGOM

Habits	Number of sizes	Range of $D_{\max}$ $[\mu\mathrm{m}]$
Sphere	24	$2-10{,}000$
Prolate spheroid	24	$2-10{,}000$
Oblate spheroid	24	$2-10{,}000$
Droxtal	24	$2-10{,}000$
Hexagonal column	24	$2-10{,}000$
Hexagonal plate	24	$2-10{,}000$
Hollow hexagonal column	24	$2-10{,}000$
6-bullet rosette	24	$2-10{,}000$
Hollow 6-bullet rosette	24	$2-10{,}000$
8-column aggregate	24	$2-10{,}000$
5-plate aggregate	24	$2-10{,}000$
10-plate aggregate	24	$2-10{,}000$

Chapter 5

Summary and outlook

5.1 Paper A

The bulk of the work presented in this paper was produced as a part of an EUMETSAT study intended to support the upcoming instruments ICI, MWI and MWS aboard the second generation of MetOp satellites. ICI will provide information on ice clouds, cirrus in particular, using channels up to $664\,$GHz including some double polarisation channels. Accurate simulations and inversions of these observations require representative enough single scattering data. However, there is currently a lack of such data that: i) include realistic complex shaped particles, especially that of large aggregates; ii) cover a frequency spectrum broad and detailed enough for the needs of ICI; and iii) include a representation of scattering properties general enough, so that polarimetric measurements can be utilized.

Accordingly, in order to cover the needs of current and future microwave missions, a general single scattering database has been developed. It consists of data covering 34 different habits (particle models), 34 frequencies from 1 to $886.4\,$GHz and 3 temperatures. Available particle sizes range from $10\,\mu$m to $2\,$cm, depending on habit. In this respect, the database is the most extensive released to this date. Covered habits range from pristine crystals such as hexagonal plates, columns, and bullet rosettes, to complex aggregates, graupel and hail. Most of the aggregate habits were generated using aggregation simulation software developed internally (by our group), using different constituent crystal axis ratios and sizes. Clear differences in scattering properties could be seen between these aggregates. Finally, scattering properties are represented using Stokes vector formalism, and are limited to totally random orientation. The database is publicly available by Zenodo, an open-access data repository operated by Cern, and is provided with data interfaces in MATLAB and Python, in order to increase the ease of use.

5.2 Paper B

Our database includes aggregates generated in a fairly realistic and sophisticated manner, for which clear differences could be discerned in terms of scattering proper-

ties. The motivation for this study is to investigate, in a more systematic manner, what aggregate aspects are important in terms of scattering properties. Using the aggregation software developed for the database, 11 simulations of aggregates with varying constituent crystal axial ratios were performed, resulting in large set of aggregate data of varying characteristics. The aggregates morphologies, and their link to the associated scattering properties were then investigated. In contrast to the database, all scattering properties are calculated assuming horizontally aligned particles.

Both radar cross-sections (at 13.4, 35.6 and 94.1 GHz) and extinction cross-sections (at 183.3, 325.2 and 664 GHz) were seen to be strongly influenced by the crystal axis ratio. The same could be said for the number of constituent crystals used in a given aggregate. Other aggregate parameters, the effective density and aerodynamic area in specific, were found to correlate strongly to the scattering properties as well. Aggregate aspect ratio was in general found to be unimportant. Furthermore, bulk properties were investigated, where the main conclusion was that multi frequency observations at both radar and sub-millimetre frequencies are affected significantly by aggregate shape. The radar triple frequency signatures, for instance, saw a clear dependence on effective density, consistent with reports from literature. Extinction at 664 GHz is relatively insensitive to shape, indicating its suitability for retrieving ice mass. It was also found that shape sensitivity of bulk properties in general is reduced if expressed in snowfall rate instead of ice water content, i.e. snowfall could potentially be retrieved at a higher accuracy than ice water content. The discoveries made here will guide future developments in aggregate representation of the database.

5.3   Outlook

There are several aspects that can be developed or considered for future work:

- The database developed in paper A is the most extensive of its kind (publicly available), but has so far seen limited exploitation and examination. Radiative transfer simulations and comparisons to measurements will be performed in the future. Findings may in turn guide the future development of the database.

- In paper A, instances of large deviations in radar back-scattering when comparing to T-matrix calculations were found in the database, in the order of tens of percents, attributed to numerical issues in the ADDA orientation averaging algorithm. To address this, portions of the data will be recalculated with increased accuracy settings at radar frequencies.

- Azimuthally random orientation could not be included into the first database version due to the associated technical issues, and was left out for a future version. For example, ARO requires impractically high storage space, in part due to the higher angle dependence compared to totally random orientation. But, we (the database developers) have already made progress on these issues, by representing the angular dependence using spherical harmonics, for instance.

On a higher level, work is needed on how to utilize the large data sizes efficiently in radiative transfer simulations.

- Liquid hydrometeors were included in the database using the Mie solution (see Sec. 3.2). A possible extension are non-spherical liquid drops, taking aero-dynamical effects on the drops into account, with azimuthally random orientation. For this, DDA must be used, though the DDA calculations will take longer time compared to ice particles, since the refractive index is much higher for water than ice at microwave frequencies.

- Scattering data of ice particles that are partially melted, were not produced due to lack of time, but is within our capability and will be included in a future version. For each habit considered, up to 5 relatively low liquid to solid ratios will be performed, likely not higher than 20 %. Particles with higher liquid content are likely not as important, as they have a shorter lifetime in the cloud (higher fall speed).

Bibliography

Auer Jr., A. H. and D. L. Veal (1970). "The Dimension of Ice Crystals in Natural Clouds". In: *J. Atmos. Sci.* 27.6, pp. 919–926.

Bailey, M. P. and J. Hallett (2009). "A comprehensive habit diagram for atmospheric ice crystals: Confirmation from the laboratory, AIRS II, and other field studies". In: *J. Atmos. Sci.* 66.9, pp. 2888–2899.

Baker, B. A. and R. P. Lawson (2006). "In Situ Observations of the Microphysical Properties of Wave, Cirrus, and Anvil Clouds. Part I: Wave Clouds". In: *J. Atmos. Sci.* 63.12, pp. 3160–3185.

Baran, A. J. (2009). "A review of the light scattering properties of cirrus". In: *J. Quant. Spectrosc. Radiat. Transfer* 110.14, pp. 1239–1260.

Baum, B. A., P. Yang, A. J. Heymsfield, C. G. Schmitt, Y. Xie, A. Bansemer, Y. X. Hu, and Z. Zhang (2011). "Improvements in shortwave bulk scattering and absorption models for the remote sensing of ice clouds". In: *J. Appl. Meteorol. Clim.* 50.5, pp. 1037–1056.

Bohren, C. F. and D. R. Huffman (1998). *Absorption and scattering of light by small particles.* New York, USA: Wiley.

Borys, R. D., D. H. Lowenthal, S. A. Cohn, and W. O. J. Brown (2003). "Mountaintop and radar measurements of anthropogenic aerosol effects on snow growth and snowfall rate". In: *Geophys. Res. Lett.* 30.10, n/a–n/a.

Buehler, S. A. et al. (2012). "Observing Ice Clouds in the Submillimeter Spectral Range: The CloudIce Mission Proposal for ESA's Earth Explorer 8". In: *Atmos. Meas. Tech.* 5, pp. 1529–1549.

Bühl, J. et al. (2017). "Remote Sensing". In: 58, pp. 10.1–10.21.

Connolly, P. J., C. Emersic, and P. R. Field (2012). "A laboratory investigation into the aggregation efficiency of small ice crystals". In: *Atmos. Chem. Phys.* 12.4, pp. 2055–2076.

Defer, E., V. S. Galligani, C. Prigent, and C. Jimenez (2014). "First observations of polarized scattering over ice clouds at close-to-millimeter wavelengths (157 GHz) with MADRAS on board the Megha-Tropiques mission". In: *J. Geophys. Res. Atmos.* 119.21, 2014JD022353.

Ding, J., L. Bi, P. Yang, G. W. Kattawar, F. Weng, Q. Liu, and T. Greenwald (2017). "Single-scattering properties of ice particles in the microwave regime: Temperature effect on the ice refractive index with implications in remote sensing". In: *J. Quant. Spectrosc. Radiat. Transfer* 190, pp. 26–37.

Draine, B. T. and P. J. Flatau (1994). "Discrete-dipole approximation for scattering calculations". In: *J. Optical Soc. o. Am. A* 11.4, pp. 1491–1499.

Eriksson, P., M. Ekström, B. Rydberg, D. L. Wu, R. T. Austin, and D. P. Murtagh (2008). "Comparison between early Odin-SMR, Aura MLS and CloudSat retrievals of cloud ice mass in the upper tropical troposphere". In: *Atmos. Chem. Phys.* 8.7, pp. 1937–1948.

Eriksson, P., M. Jamali, J. Mendrok, and S. A. Buehler (2015). "On the microwave optical properties of randomly oriented ice hydrometeors". In: *Atmos. Meas. Tech.* 8.5, pp. 1913–1933.

Eriksson, P., B. Rydberg, H. Sagawa, M. S. Johnston, and Y. Kasai (2014). "Overview and sample applications of SMILES and Odin-SMR retrievals of upper tropospheric humidity and cloud ice mass". In: *Atmos. Chem. Phys.* 14.23, pp. 12613–12629.

Fabry, F. and I. Zawadzki (1995). "Long-Term Radar Observations of the Melting Layer of Precipitation and Their Interpretation". In: *J. Atmos. Sci.* 52.7, pp. 838–851.

Field, P. R., A. J. Heymsfield, and A. Bansemer (2006). "Shattering and particle interarrival times measured by optical array probes in ice clouds". In: *J. Atmos. Oceanic Technol.* 23.10, pp. 1357–1371.

Field, P. R., A. J. Heymsfield, and A. Bansemer (2007). "Snow size distribution parameterization for midlatitude and tropical ice clouds". In: *J. Atmos. Sci.* 64.12, pp. 4346–4365.

Fujiyoshi, Y. (1986). "Melting Snowflakes". In: *J. Atmos. Sci.* 43.3, pp. 307–311.

Garrett, T. J., S. E. Yuter, C. Fallgatter, K. Shkurko, S. R. Rhodes, and J. L. Endries (2015). "Orientations and aspect ratios of falling snow". In: *Geophys. Res. Lett.* 42.11, pp. 4617–4622.

Geer, A. J. and F. Baordo (2014). "Improved scattering radiative transfer for frozen hydrometeors at microwave frequencies". In: *Atmos. Meas. Tech.* 7.6, pp. 1839–1860.

Geer, A. J., F. Baordo, N. Bormann, P. Chambon, S. J. English, M. Kazumori, H. Lawrence, P. Lean, K. Lonitza, and C. Lupu (2017). "The growing impact of satellite observations sensitive to humidity, cloud and precipitation". In: *Q. J. R. Meteorol. Soc.* 143.709, pp. 3189–3206.

Gong, J. and D. L. Wu (2017). "Microphysical properties of frozen particles inferred from Global Precipitation Measurement (GPM) Microwave Imager (GMI) polarimetric measurements". In: *Atmos. Chem. Phys.* 17, pp. 2741–2757.

Gravner, J. and D. Griffeath (2009). "Modeling snow-crystal growth: a three-dimensional mesoscopic approach". In: *Phys. Rev.* 79E.011601.

Heymsfield, A. J. and M. Kajikawa (1987). "An Improved Approach to Calculating Terminal Velocities of Plate-like Crystals and Graupel". In: *J. Atmos. Sci.* 44.7, pp. 1088–1099.

Heymsfield, A. J., S. Lewis, A. Bansemer, J. Iaquinta, L. M. Miloshevich, M. Kajikawa, C. Twohy, and M. R. Poellot (2002). "A general approach for deriving the properties of cirrus and stratiform ice cloud particles". In: *J. Atmos. Sci.* 59, pp. 3–29.

Heymsfield, A. J. and L. M. Miloshevich (2003). "Parameterizations for the cross-sectional area and extinction of cirrus and stratiform ice cloud particles". In: *J. Atmos. Sci.* 60.7, pp. 936–956.

Heysmfield, A. J., C. Schmitt, A. Bansemer, and C. H. Twohy (2010). "Improved representation of ice Particle masses based on observations in natural clouds". In: *J. Appl. Meteorol. Clim.* 67, pp. 3303–3318.

Hobbs, P. V., S. Chang, and J. D. Locatelli (1974). "The dimensions and aggregation of ice crystals in natural clouds". In: *J. Geophys. Res.* 79.15, pp. 2199–2206.

Hong, G., P. Yang, B. A. Baum, A. J. Heymsfield, F. Weng, Q. Liu, G. Heygster, and S. A. Buehler (2009). "Scattering database in the millimeter and submillimeter wave range of 100-1000 GHz for nonspherical ice particles". In: *J. Geophys. Res.* 114, D06201, p. 6201.

Hosler, C. L., D. C. Jensen, and L. Goldshlak (1957). "On the aggregation of ice crystals to form snow". In: *J. Meteorol.* 14.5, pp. 415–420.

Hou, A. Y., R. K. Kakar, S. Neeck, A. A. Azarbarzin, C. D. Kummerow, M. Kojima, R. Oki, K. Nakamura, and T. Iguchi (2014). "The Global Precipitation Measurement Mission". In: *Bull. Amer. Met. Soc.* 95.5, pp. 701–722.

Hudak, D., W. Petersen, G. Skofronick-Jackson, M. Wolde, M. Schwaller, P. Joe, C. Derksen, K. Strawbridge, P. Kollias, and R. Stewart (2012). "GPM cold season precipitation experiment (GCPEx)". In: *EUMETSAT Proc. Meteor. Sat. Conf., Sopot, Poland*, pp. 1–8.

Hulst, H. C. van de (1957). *Light scattering by small particles.* New York : Dover Publications, inc.

IPCC (2007). *Climate Change 2007: The Physical Science Basis. Contribution of Working Group I to the Fourth Assessment Report of the Intergovernmental Panel on Climate Change.* Ed. by S. Solomon, D. Qin, M. Manning, Z. Chen, M. Marquis, K.B. Averyt, M. Tignor, and H.L. Miller. Cambridge, United Kingdom and New York, NY, USA: Cambridge University Press.

IPCC (2013). "Clouds and Aerosols". In: *Climate Change 2013: The Physical Science Basis. Contribution of Working Group I to the Fifth Assessment Report of the Intergovernmental Panel on Climate Change.* Ed. by T.F. Stocker, D. Qin, G.-K. Plattner, M. Tignor, S.K. Allen, J. Boschung, A. Nauels, Y. Xia, V. Bex, and P.M. Midgley. Cambridge, United Kingdom and New York, NY, USA: Cambridge University Press. Chap. 7, pp. 571–658.

Iwabuchi, H. and P. Yang (2011). "Temperature dependence of ice optical constants: Implications for simulating the single-scattering properties of cold ice clouds". In: *J. Quant. Spectrosc. Radiat. Transfer* 112.15, pp. 2520–2525.

Jiang, J. H. and D. L. Wu (2004). "Ice and water permittivities for millimeter and sub-millimeter remote sensing applications". In: *Atm. Sci. Lett.* 5, pp. 146–151.

Johnson, B. T., W. S. Olson, and G. Skofronick-Jackson (2016). "The microwave properties of simulated melting precipitation particles: sensitivity to initial melting". In: *Atmos. Meas. Tech.* 9.1, pp. 9–21.

Kahnert, M. (2015). "Numerical solutions of the macroscopic Maxwell equations for scattering by non-spherical particles: A tutorial review". In: *J. Quant. Spectrosc. Radiat. Transfer.* in press.

Kajikawa, M. (1972). "Measurement of Falling Velocity of Individual Snow Crystals". In: *J. Meteorol. Soc. Jpn.* 50.6, pp. 577–584.

Kangas, V., S. D'Addio, M. Betto, H. Barré, and G. Mason (2012). "MetOp Second Generation Microwave radiometers". In: *2012 12th Specialist Meeting on Microwave Radiometry and Remote Sensing of the Environment (MicroRad)*, pp. 1–4.

Kikuchi, K., T. Kameda, K. Higuchi, and A. Yamashita (2013). "A global classification of snow crystals, ice crystals, and solid precipitation based on observations from middle latitudes to polar regions". In: *Atmos. Res.* 132-133.January 1969, pp. 460–472.

Korolev, A. V., E. F. Emery, J. W. Strapp, S. G. Cober, G. A. Isaac, M. Wasey, and D. Marcotte (2011). "Small ice particles in tropospheric clouds: Fact or artifact? Airborne Icing Instrumentation Evaluation Experiment". In: *Bull. Amer. Met. Soc.* 92.8, p. 967.

Korolev, A. V., G. A. Isaac, and J. Hallett (1999). "Ice particle habits in Arctic clouds". In: *Geophys. Res. Lett.* 26.9, pp. 1299–1302.

Korolev, A. and G. Isaac (2003). "Roundness and aspect ratio of particles in ice clouds". In: *J. Atmos. Sci.* 60.15, pp. 1795–1808.

Kuhn, T. and I. Gultepe (2016). "Ice Fog and Light Snow Measurements Using a High-Resolution Camera System". In: *Pure Appl. Geophys.* 173.9, pp. 3049–3064.

Kuhn, T. and A. J. Heymsfield (2016). "In Situ Balloon-Borne Ice Particle Imaging in High-Latitude Cirrus". In: *Pure Appl. Geophys.* 173.9, pp. 3065–3084.

Kulie, M. S., R. Bennartz, T. J. Greenwald, Y. Chen, and F. Weng (2010). "Uncertainties in microwave properties of frozen precipitation: Implications for remote sensing and data assimilation". In: *J. Atmos. Sci.* 67.11, pp. 3471–3487.

Kuo, K.-S., W. S. Olson, B. T. Johnson, M. Grecu, L. Tian, T. L. Clune, B. H. van Aartsen, A. J. Heymsfield, L. Liao, and R. Meneghini (2016). "The Microwave Radiative Properties of Falling Snow Derived from Nonspherical Ice Particle Models. Part I: An Extensive Database of Simulated Pristine Crystals and Aggregate Particles, and Their Scattering Properties". In: *J. Appl. Meteorol. Clim.* 55.3, pp. 691–708.

Latham, J. (1969). *Cloud physics*. Vol. 32. 1. IOP Publishing, p. 302.

Lawson, R. P., B. A. Baker, C. G. Schmitt, and T. L. Jensen (2001). "An overview of microphysical properties of Arctic clouds observed in May and July 1998 during FIRE ACE". In: *J. Atmos. Sci.* 106014.27, pp. 989–15.

Lawson, R. P., B. A. Baker, P. Zmarzly, D. O'Connor, Q. Mo, J.F. Gayet, and V. Shcherbakov (2006). "Microphysical and optical properties of atmospheric ice crystals at South Pole Station". In: *J. Appl. Meteorol. Clim.* 45.11, pp. 1505–1524.

Lindqvist, H., K. Muinonen, T. Nousiainen, J. Um, G. M. McFarquhar, P. Haapanala, R. Makkonen, and H. Hakkarainen (2012). "Ice-cloud particle habit classification using principal components". In: *J. Geophys. Res. Atmos.* 117.D16.

Liu, G. (2008). "A database of microwave single-scattering properties for nonspherical ice particles". In: *Bull. Amer. Met. Soc.* 89, p. 1563.

Lu, Y., Z. Jiang, K. Aydin, J. Verlinde, E. E. Clothiaux, and G. Botta (2016). "A polarimetric scattering database for non-spherical ice particles at microwave wavelengths". In: *Atmos. Meas. Tech.* 9, pp. 5119–5134.

Magono, C. and C. W. Lee (1966). "Meteorological classification of natural snow crystals". In: *Journal of the Faculty of Science, Hokkaido University. Series 7, Geophysics* 2.4, pp. 321–335.

Mätzler, C. (2006). "Thermal Microwave Radiation: Application for Remote Sensing". In: vol. 52. IET Electromagn. Waves Ser. Inst. Eng. Technol., Stevenage, U. K. Chap. 5.3 Microwave dielectric properties of ice, pp. 455–462.

May, P. T., J. H. Mather, G. Vaughan, C. Jakob, G. M. McFarquhar, K. N. Bower, and G. G. Mace (2008). "The tropical warm pool international cloud experiment". In: *Bull. Amer. Met. Soc.* 89.5, p. 629.

McFarquhar, G. M., D. Baumgardner, and A. J. Heymsfield (2017). "Background and Overview". In: 58, pp. v–ix.

McFarquhar, G. M. and A. J. Heymsfield (1997). "Parameterization of tropical cirrus ice crystal size distribution and implications for radiative transfer: Results from CEPEX". In: *J. Atmos. Sci.* 54, pp. 2187–2200.

McFarquhar, G. M., S. Ghan, J. Verlinde, A. Korolev, J. W. Strapp, B. Schmid, J. M. Tomlinson, M. Wolde, S. D. Brooks, D. Cziczo, et al. (2011). "Indirect and semi-direct aerosol campaign: The impact of Arctic aerosols on clouds". In: *Bull. Amer. Met. Soc.* 92.2, p. 183.

Mie, G. (1908). "Beiträge zur optik trüber medien, speziell kolloidaler metallösungen". In: *Annalen der Physik* 330.3, pp. 377–445.

Mishchenko, M. I. and L. D. Travis (1998). "Capabilities and limitations of a current FORTRAN implementation of the T-matrix method for randomly oriented, rotationally symmetric scatterers". In: *J. Quant. Spectrosc. Radiat. Transfer* 60.3, pp. 309–324.

Mishchenko, M. I., L. D. Travis, and D. W. Mackowski (1996). "T-matrix computation of light scattering by nonspherical particles: A review". In: *J. Quant. Spectrosc. Radiat. Transfer* 55.5, pp. 535–575.

Mishchenko, M. I., L.D. Travis, and A.A. Lacis (2002). *Scattering, absorption, and emission of light by small particles.* Cambridge, UK: Cambridge University Press.

Mitchell, D. L. (1996). "Use of Mass- and Area-Dimensional Power Laws for Determining Precipitation Particle Terminal Velocities". In: *J. Atmos. Sci.* 53.12, pp. 1710–1723.

Mitchell, D. L. and W. P. Arnott (1994). "A Model Predicting the Evolution of Ice Particle Size Spectra and Radiative Properties of Cirrus Clouds. Part II: Dependence of Absorption and Extinction on Ice Crystal Morphology". In: *J. Atmos. Sci.* 51.6, pp. 817–832.

Mitchell, D. L., R. P. Lawson, and S. Mishra (2011). *Cirrus clouds and climate engineering: new findings on ice nucleation and theoretical basis.* INTECH Open Access Publisher.

Mitchell, D. L., R. Zhang, and R. L. Pitter (1990). "Mass-Dimensional Relationships for Ice Particles and the Influence of Riming on Snowfall Rates". In: *J. Appl. Meteorol.* 29.2, pp. 153–163.

Mitra, S. K., O. Vohl, M. Ahr, and H. R. Pruppacher (1990). "A Wind Tunnel and Theoretical Study of the Melting Behavior of Atmospheric Ice Particles. IV: Experiment and Theory for Snow Flakes". In: *J. Atmos. Sci.* 47.5, pp. 584–591.

Nowell, H., G. Liu, and R. Honeyager (2013). "Modeling the microwave single-scattering properties of aggregate snowflakes". In: *J. Geophys. Res.* 118, pp. 7873–7885.

Oraltay, R. G., J. Hallett, R. G. Oraltay, and J. Hallett (2005). "The Melting Layer: A Laboratory Investigation of Ice Particle Melt and Evaporation near 0°C". In: *J. Appl. Meteorol.* 44.2, pp. 206–220.

Orikasa, N., M. Murakami, and A. J. Heymsfield (2013). "Ice crystal concentration in midlatitude cirrus clouds: In situ measurements with the balloonborne hydrometeor videosonde (HYVIS)". In: *J. Meteorol. Soc. Jpn.* 91.2, pp. 143–161.

O'Shea, S. J., T. W. Choularton, G. Lloyd, J. Crosier, K. N. Bower, M. Gallagher, S. J. Abel, R. J. Cotton, P. R. A. Brown, J. P. Fugal, et al. (2016). "Airborne observations of the microphysical structure of two contrasting cirrus clouds". In: *J. Geophys. Res. Atmos.*

Petty, G. W. and W. Huang (2011). "The Modified Gamma Size Distribution Applied to Inhomogeneous and Nonspherical Particles: Key Relationships and Conversions". In: *J. Atmos. Sci.* 68.7, pp. 1460–1473.

Ray, P. S. (1972). "Broadband complex refractive indices of ice and water". In: *Appl. Opt.* 11, pp. 1836–1844.

Rees, W. G. (2012). *Physical principles of remote sensing*. Cambridge university press.

Saleh, B. E. A. and M. C. Teich (2007). *Fundamentals of photonics*. Wiley New York.

Schulz, F. M., K. Stamnes, and J. J. Stamnes (1998). "Scattering of electromagnetic waves by spheroidal particles: a novelapproach exploiting the T matrix computed in spheroidalcoordinates". In: *Appl. Opt.* 37.33, pp. 7875–7896.

Stephens, G. L. et al. (2002). "THE CLOUDSAT MISSION AND THE A-TRAIN". In: *Bull. Amer. Met. Soc.* 83.12, pp. 1771–1790. eprint: `https://doi.org/10.1175/BAMS-83-12-1771`.

Storelvmo, T. and I. Tan (2015). "The Wegener-Bergeron-Findeisen process - Its discovery and vital importance for weather and climate". In: *Meteorologische Zeitschrift* 24.4, pp. 455–461.

Stubenrauch, C. J. et al. (2013). "Assessment of Global Cloud Datasets from Satellites: Project and Database Initiated by the GEWEX Radiation Panel". In: *Bull. Amer. Met. Soc.* 94.7, pp. 1031–1049.

Troitsky, A. V., A. M. Osharin, A. V. Korolev, and J. W. Strapp (2003). "Polarization of Thermal Microwave Atmospheric Radiation Due to Scattering by Ice Particles in Clouds". In: *J. Atmos. Sci.* 60.13, pp. 1608–1620.

Tyynelä, J., J. Leinonen, D. Moisseev, T. Nousiainen, and A. von Lerber (2014). "Modeling radar backscattering from melting snowflakes using spheroids with nonuniform distribution of water". In: *J. Quant. Spectrosc. Radiat. Transfer* 133, pp. 504–519.

Um, J. and G. M. McFarquhar (2009). "Single-scattering properties of aggregates of plates". In: *Q. J. R. Meteorol. Soc.* 135.639, pp. 291–304.

Um, J., G. M. McFarquhar, Y. P. Hong, S. S. Lee, C. H. Jung, R. P. Lawson, and Q. Mo (2015). "Dimensions and aspect ratios of natural ice crystals". In: *Atmos. Chem. Phys.* 15, pp. 3933–56.

Wallace, J. M. and P. V. Hobbs (2006). *Atmospheric science: an introductory survey.* Vol. 92. Academic press.

Warren, S. (1984). "Optical constants of ice from the ultraviolet to the microwave". In: *Appl. Opt.* 23, pp. 1206–1225.

Warren, S. G. and R. E. Brandt (2008). "Optical constants of ice from the ultraviolet to the microwave: A revised compilation". In: *J. Geophys. Res.* 113, D14220.

Waterman, P. C. (1965). "Matrix formulation of electromagnetic scattering". In: *Proc. IEEE* 53.8, pp. 805–812.

Webster, P. J., V. O. Magana, T. N. Palmer, J. Shukla, R. A. Tomas, M. U. Yanai, and T. Yasunari (1998). "Monsoons: Processes, predictability, and the prospects for prediction". In: *J. Geophys. Res. Ocea.* 103.C7, pp. 14451–14510.

Westbrook, C. D., R. C. Ball, P. R. Field, and A. J. Heymsfield (2004). "Theory of growth by differential sedimentation, with application to snowflake formation". In: *Phys. Rev. E* 70.2, p. 021403.

Wu, D. L., R. T. Austin, M. Deng, S. L. Durden, A. J. Heymsfield, J. H. Jiang, A. Lambert, J.-L. Li, N. J. Livesey, G. M. McFarquhar, et al. (2009). "Comparisons of global cloud ice from MLS, CloudSat, and correlative data sets". In: *J. Geophys. Res. Atmos.* 114.D8.

Wylie, D., D. L. Jackson, W. P. Menzel, and J. J. Bates (2005). "Trends in Global Cloud Cover in Two Decades of HIRS Observations". In: *J. Climate* 18.15, pp. 3021–3031.

Xie, X., U. Löhnert, S. Kneifel, and S. Crewell (2012). "Snow particle orientation observed by ground-based microwave radiometry". In: *J. Geophys. Res.* 117.D2.

Xu, Y.-L. (1995). "Electromagnetic scattering by an aggregate of spheres". In: *Appl. Opt.* 34.21, p. 4573.

Yang, P., L. Bi, B. A. Baum, K.-N. Liou, G. W. Kattawar, M. I. Mishchenko, and B. Cole (2013). "Spectrally Consistent Scattering, Absorption, and Polarization Properties of Atmospheric Ice Crystals at Wavelengths from 0.2 to 100 μm". In: *J. Atmos. Sci.* 70.1, pp. 330–347.

Yang, P. and K. N. Liou (1996). "Geometric-optics–integral-equation method for light scattering by nonspherical ice crystals". In: *Appl. Opt.* 35.33, pp. 6568–6584.

Yurkin, M. A. and A. G. Hoekstra (2014). *User Manual for the Discrete Dipole Approximation Code ADDA 1.3b4.*

Zhang, C., K.-S. Lee, X.-C. Zhang, X. Wei, and Y.R. Shen (2001). "Optical constants of ice Ih crystal at terahertz frequencies". In: *Appl. Phys. Lett.* 79.4, pp. 491–493.

Zhang, K., X. Liu, M. Wang, J. M. Comstock, D. L. Mitchell, S. Mishra, and G. G. Mace (2013). "Evaluating and constraining ice cloud parameterizations in CAM5 using aircraft measurements from the SPARTICUS campaign". In: *Atmos. Chem. Phys.* 13.9, pp. 4963–4982.